4-5-2019

Thermophysical Properties and Characterization of Diamond Silicon Carbide

Alexandra Merkouriou
alexandra.merkouriou@uconn.edu

Thermophysical Properties and Characterization of Diamond Silicon Carbide

Alexandra Merkouriou

B.S. University of Connecticut, 2015

A Thesis

Submitted in Partial Fulfillment of the

Requirements for the Degree of

Master of Science

At the

University of Connecticut

2019

APPROVAL PAGE

Master of Science Thesis

Thermophysical Properties and Characterization of

Diamond Silicon Carbide

Presented by

Alexandra Merkouriou, B.S.

Major Advisor _____

Dr. Pamir Alpay

Associate Advisor _____

Dr. Rainer Hebert

Associate Advisor _____

Dr. Lesley Frame

University of Connecticut

2019

Acknowledgements

First, I would like to thank Dr. Alpay for mentoring and advising me through both my undergraduate and graduate career. He continues to help me attain goals I did not think were reachable.

I would like to thank Mike Aghajanian and M Cubed Technologies for providing the resources necessary for making this work possible. I would also like to thank Al McCormick for motivating me to work with precision and purpose to ensure the most thorough results possible. I would like to thank Matt Stevens and Ed Gratrix for encouraging me along the way. I would like to thank Rob Campbell from Netzsch for tirelessly helping me with and teaching me about laser flash analysis as it related to my samples.

I would like to thank Ben Bedard for being the best friend anyone could have during this entire process, from classes to thesis writing and everything in between. I would also like to thank Ben for his help with all of the fantastic SEM and VLM images in this thesis as they would not be possible without him.

I would like to thank Simon Hobbs for always finding a good study spot and helping in every way he knew how.

I would like to thank Austin McDannald for being a friend and mentor, and for encouraging me to dive into the rabbit hole for all things in science and in life.

Last but not least, I would like to thank my parents for always believing in me and making absolutely sure that I saw my masters work to completion.

List of Figures

Table of Contents

Abstract

Heat dissipation is a growing concern for multiple industries as technologies advance and is driving the need for materials with higher thermal conductivity than copper (400W/mK at room temperature[1]) that can be made at reasonable manufacturing costs in a variety of shapes and sizes.[2,3] Such advancements include metal and ceramic matrix composites with a diamond particulate phase such diamond silicon carbide (SiC). In this work, eight different particle sizes of diamond ranging from 22 μm to 500 μm were infiltrated with liquid silicon in a binder-less casting process to reduce the internal stress that results from binder migration and to determine the effect of particulate size on the thermophysical properties. In this process, the liquid silicon reacts with the diamond to form a SiC matrix phase, however, micrographs expose the creation of pores resulting from this process as well. X-ray diffraction results confirm the formation of β-SiC as well as diamond and silicon phases across the range of samples. Laser flash analysis was used to measure the thermal diffusivity of samples sliced to thicknesses of 0.5 mm and 5 mm allowing for an investigation of the thermal properties on both bulk and non-bulk materials. Thermal conductivity calculations revealed that the non-bulk samples out preformed the bulk samples with thermal conductivities ranging from 303 W/mK to 641 W/mK and 283 W/mK to 542 W/mK respectively. In conclusion, diamond particle sizes of 65 μm or higher achieve thermal conductivities superior to copper when produced using binder-less liquid silicon infiltration. However, there is room to improve processing parameters to reduce defects and create a more uniform material.

Chapter 1 Introduction

1.1 The Development of Synthetic Diamond

The history of diamonds is one of both progress and conflict. As many as eight thousand years ago, diamonds were found along the coasts of the Krishna and Godavaria rivers in India. Here, they were used as decorations for religious icons as well as for some of the first engraving tools. It was at this point that diamonds were first established as a sign of wealth and status.

It was not until one thousand years ago, though, that the diamond trade industry began with Venice and Bruges emerging as centers for diamond trade throughout Europe. By the eighteenth-century India's diamond supply had largely run out and the center for diamond exports shifted to Brazil and Africa. Not long after, Cecil Rhodes founded the de Beers mining company which quickly grew to dominate 90% of the diamond market and cement diamonds as a staple of romance.[4]

Meanwhile, by 1797 technical interest in diamonds was sparked when Smithson Tennant discovered that diamond could indeed burn, something that was previously hypothesized as impossible by Newton. Tennant concluded that though diamond was much harder, it must be entirely comprised of charcoal in a different crystallized form.[5] Later scientists would prove that charcoal and diamond were both forms of carbon and the race to turn graphite into diamond began. However, it wasn't until over 100 years later with the development of thermodynamics and the pressure-temperature carbon phase diagram that any progress was made. It was theorized that if pressures of 60 kilobars could be reached at temperatures of 600 ˚C it may be possible to create synthetic diamond. However, reaching these pressures proved challenging, limiting efforts. Demand for synthetic diamond grew with World War II in the 1940's due to its efficacy at grinding tungsten carbide for cutting tool and armor-piercing rounds. Such demand then sparked a

collaboration between Zay Jeffries of General Electric (GE) and Harvard Professor and Nobel Prize winning Percy Bridgeman. Jeffries' work at GE developing tungsten carbide gave Bridgeman a new material capable of creating higher pressure environments than ever previously produced in an effort to chase the graphite to diamond transition zone. Unfortunately, the synthetic diamond remained elusive.[6]

GE did not officially invest in the effort to make synthetic diamonds until 1950. Instead of partnering with The Norton Company, GE funded its own team of scientists to work out the problem using both high pressure and high temperature synthesis as well as other techniques at lower pressures. Initial success with the low-pressure techniques would later be found to be in error, but by 1955 H. Tracy Hall and team discovered a successful method to create synthetic diamond. They first created a belted pressure vessel noting that a single stage process was essential if synthetic diamonds were ever to be commercially manufacturable. After adding an iron catalyst to their belted furnace design they were able to reach a pressure of 75 kilobars at a temperature of 1200˚C, and alas transparent and isotropic diamond crystals formed.[6]

The main disadvantages to the high-pressure high-temperature (HPHT) method of diamond growth developed by GE are high equipment and energy costs and diamond particle size. HPHT manufacturing can only produce diamonds in the range of nanometer to micron diameters thus limiting the number of applications. An alternative to HPHT processing that helps to solve these two major disadvantages is chemical vapor deposition (CVD). This process involves an atomized hydrogen gas phase chemical reaction over a solid surface or substrate, usually made of tantalum and at temperatures of 700˚C and above the chemical reaction produces diamond growth on the substrate anywhere from 1 to 10 μm/hour depending on the reactor setup being used. Crystals nucleate on the substrate and eventually grow in three dimensions to form a film. After that, all

growth must proceed in a vertical direction and a polycrystalline columnar structure with many grain boundaries and defects is produced. As the diamond grows thicker in the z-direction, the grains also grow, and the number of defects and grain boundaries are reduced. Diagrams of common CVD apparatuses are shown in the figure below, with one common limiting factor of CVD diamond growth being its corrosion of the substrate and reactors. This causes metal impurities in the diamond making it unviable for applications outside of the mechanical processing realm.[2]

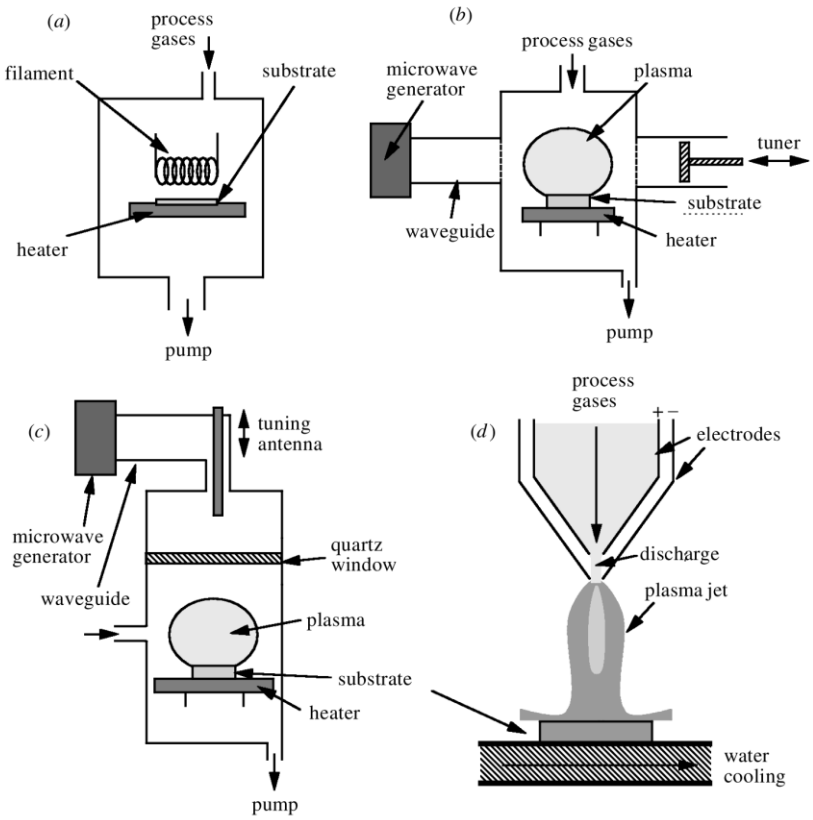

Figure 1.1 Common CVD apparatuses. (a) depicts hot filament CVD, (b) depicts a 'NIRIM-type' microwave plasma reactor, (c) depicts an 'ASTEX-type' microwave plasma reactor, and (d) depicts a DC arc jet reactor, or plasma torch.[2]

Diamonds are classified into four categories. Type Ia diamond is the most common form of natural diamond, accounting for 95% - 98% of diamonds mined from the earth. Type Ia diamond is characterized by up to a 0.2% substitutional nitrogen impurity that forms in aggregates or platelets and has a low thermal conductivity (less than 9 W/mK) and high electrical resistivity

(greater than 10^4 Ωm). Like Type Ia diamond, Type Ib diamond also has a dispersed nitrogen impurity which frequently produces a yellow or slightly green color in the diamond. Type Ib diamond is the most common form of industrial diamond and is consequently the type of diamond used in this study. The last two categories of diamond are free of nitrogen impurities. Type IIa diamond is gem stone quality diamond and has the highest thermal conductivity and electrical resistivity seen in diamonds, upwards of 2000 W/mK and 10^{14} Ωm respectively. Lastly, type IIb diamond is defined by having boron impurities. Natural diamond typically has 0.25 ppm of boron impurities while synthetic diamond can have up to 270 ppm, giving it a slightly blue color. Due to this boron impurity, type IIb diamond exhibits p-type conductivity and an electrical resistance of 0.1 to 100 Ωm.[7]

Today, diamonds are used in a variety of applications and industries. The high wear resistance of diamond offers an advantage in metal bonded diamonds for machine tooling applications. This has revolutionized the stone, drilling, and civil engineering industries as the diamonds allow for more efficient machining as compared to tradition hardened metal tools.[8,9] The high corrosion resistance and broad transparency of diamond are ideal for the optical industry and allow diamonds to be used as windows, especially in corrosive environments.[10] Diamond thin films are even being used as a substrate to integrate microelectronics and biological sensing.[11] However, the property most widely leveraged, and the property this study investigates, is the high thermal conductivity of diamond. With the growth of high-power electronics and opto-electronic devices, thermal management has become an ever-increasing issue. Diamond offers a thermal conductivity of 2000 W/mK, five times that of copper, to help solve heating issues in integrated circuits, low powered laser diodes and even GaN LEDs.[2,12] In spite of the advancements of both HPHT and

CVD diamond production, manufacturability remains a challenge. Thus, the development of metal and ceramic based diamond composites is an area of increasing interest.

1.2 Ceramic Processing Methods

The evolution of human history is closely integrated with ceramics, with the earliest known ceramics being fired figures created in 22,000 B.C. In the time since then, significant advancements have been made in the ceramic processing industry, but the general procedure remains relatively unchanged. First a green body ceramic must be made. A green body is a combination of ceramic powders and additives, or binders, that create a slurry and hold the ceramic powders in the desired shape until the part can be sintered, fired, or infiltrated. Green bodies can be made by slip casting, filter pressing, tape casting and sediment casting, among other methods, depending on the desired final shape and density of the part. In general, slip casting and filter casting produce lower density ceramics while tape casting can be used to create thin stacked layers allowing for the production of integrated circuits. After the slurry is made for sediment casting it is poured into molds and allowed to settle. As the ceramic powders settle, they sink to the bottom and the liquid pools at the top of the mold. The liquid is then removed, and the compacted powders are allowed to dry, which produces high density green bodies.[13]

After the green bodies have been cast and dried, it is time for sintering or densification. This is a process that serves to fill the porous network of the green body. Reactive sintering occurs when a phase transformation or chemical reaction takes place in conjunction with the sintering process. This is a common method for producing metal matrix composites, including those with diamonds as a dispersed phase.[13] Besides the need for thermal processing, the one thing that these techniques have in common is the addition of the aforementioned binder. Binders come in two forms, inorganic and organic. Inorganic binders include powders or resins like phenolic. One major

disadvantage of inorganic binders is their toxicity if not handled correctly. The fumes of phenolic, for example, contain formaldehyde which is a known carcinogen. Additionally, phenolic powder can react with air and explode with less heat needed than to boil water.[14,15] While organic binders are less adverse for one's health, they have their own major disadvantage known as binder migration.

Binder migration is a problem that plagues the ceramics industry, especially when ceramics are sediment cast. Binder migration was defined as early as 1945 by Comeforo as the movement of the binder to the top of the work piece during the drying process.[16] This causes an uneven distribution of stress in the green body which is later translated to the sintered part, overall causing warping and possible cracking.[13] As the ceramic industry grows, the applications affected by binder migration also increases. In more recent times, binder migration has expanded to applications such as Li ion batteries, as Front observed that binder migration resulted in increased resistivity and therefore decreased cell capacity in the Li ion batteries. After conducting experiments examining the effect of the drying rate on binder migration, Front concludes that lower drying rates produce a more homogenous binder distribution while high drying rates produce a concentration of binder at the evaporating surface. However, prolonged drying times are not favorable to manufacturing outputs. Thus, in order to achieve the best production throughput while mitigating binder migration, Front suggests that a high drying rate should be used in the begging of the drying cycle and a low drying rate should be used towards the end.[17]

While this reduces the amount of binder migration in the ceramic it does not eliminate its effects completely. Thus, one element tested in the experimental design discussed here is a binder-less process for casting ceramic materials; specifically, diamond-silicon carbide.

Chapter 2 Methods

2.1 Sample Preparation

This study focuses on eight different varieties of a diamond silicon carbide material, otherwise referred to as Thermadite®. Each sample is unique in the diamond particle size used to create it. Particle sizes range from 22 μm for Sample A to 500 μm for sample H, as shown in **Error! Reference source not found.**.

Table 2.1 Diamond sample name as related to mesh size, average particle size and grade.

Sample Name	Mesh Size	Average Particle Size (um)	Grade
A	500/600	22	MBD6
B	325/400	45	MBD6
C	230/270	65	MBD6
D	140/170	100	MBD6
E	100/120	150	MBD6
F	70/80	212	MBD6
G	45/50	355	MBD6
H	35/40	500	SMD25

The MBD6 and SMD 25 grades were chosen due to their particle size and shape uniformity as compared to other grades. The grade of SMD25 was chosen for Sample H because it was the only diamond grade available from the supplier with the large particle size of 500 μm. A representative image of the particle shape uniformity for the diamond used in these experiments is shown in the figure below.

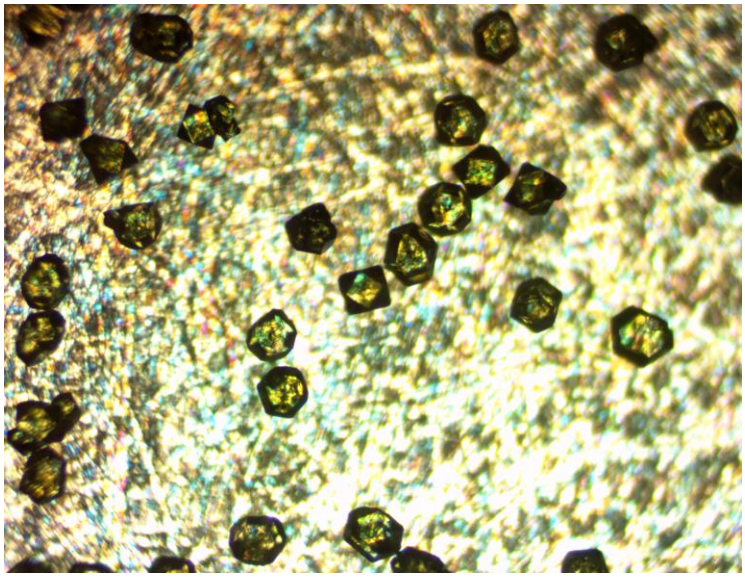

Figure 2.1 Representative image of uniform diamond shape. The sample shown here is Sample E, 150 μm particles.

After choosing the particle sizes, 50.8 mm diameter by 12.7 mm tall disk-shaped samples were made by infiltrating the diamond with high purity liquid silicon at approximately 1500˚C in a vacuum atmosphere. Figure 2.2 shows the infiltrated disks beginning with Sample A (22 μm) on the top left and continuing left to right until Sample H (500 μm) on the bottom right. The Archimedes method was used to calculate density on the bulk samples, using the equation below.

$$\rho_s = \frac{m_d \rho_{H_2O}}{m_d - m_w} \qquad 2.1$$

Where ρ_s is the density of the diamond sample (g/cm^3), m_d is the mass of the dry sample (g), ρ_{H2O} at 20 ˚C is 0.9982336 is the relative density of water at 20 ˚C,[18] and m_w is the mass of the wet sample (g).

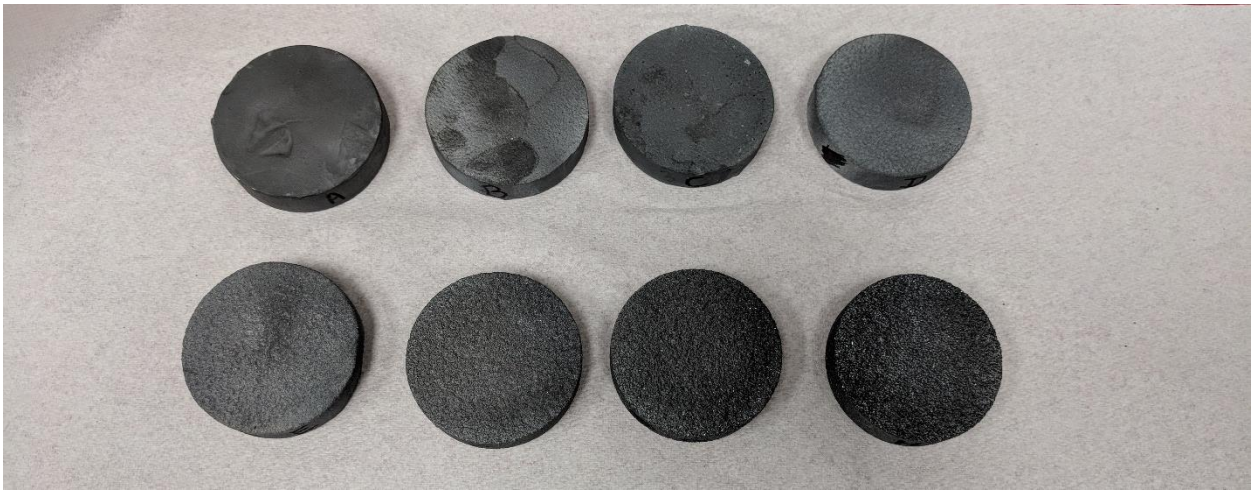

Figure 2.2 Diamond samples post infiltration. Seen at the top row on the left is Sample A (22 μm), Sample B (45 μm), Sample C (65 μm) and Sample D (100 μm). Continuing with the bottom row on the left is Sample E (150 μm), Sample F (212 μm), Sample G (355 μm) and Sample H (500 μm).

The bulk material samples were precisely cut into smaller shapes for use in analysis by the Synova Laser MicroJet technology. A 3-axis LDS 200 Synova MicroJet laser was used to cut the samples into 12.7 mm diameter cylinders. A 5-axis Synova LCS 50 MicroJet laser was subsequently used to slice the cylinders into disks with 0.5 mm and 5 mm thickness.[19] Two samples per thickness per diamond particle size were cut for a total of 32 samples.

The exceptional sample quality of the Synova Microjet technology is shown by the dimensional accuracy, parallelism and surface finish of the 32 as cut pieces. This technology makes use of a ND:YAG fiber laser with micro or nano second pulse widths with the end of the fiber projected into a diamond or sapphire nozzle after various demagnification and focusing lenses. However, the key to this technology lies in the filtered and deionized (DI) water chamber that sits above the nozzle, as seen in Figure 2.3. Due to the refractive index of the water stream, the laser beam undergoes total internal reflection at the water-air interface. This allows the stream to act as an optical fiber, thus avoiding the de-focusing issues seen in conventional laser beam delivery. Additional advantages of Synova MicroJet technology over conventional mechanical diamond processing techniques and other laser machining methods are numerous. First, the

internal reflection and laminar flow of water allows for focusing of the laser beam thus producing parallel side walls in the material being cut. The water coupled with the pulsing laser allows for a low temperature operation which has less thermal impact on the surface structure of the material as compared to conventional lasers. Moreover, the low force of the stream of water expels any recast material that may have solidified on the sample. These advantages combined with 3 μm precision on a x-y stage allows for accurate cutting of otherwise difficult to machine materials such as diamond.[20–22]

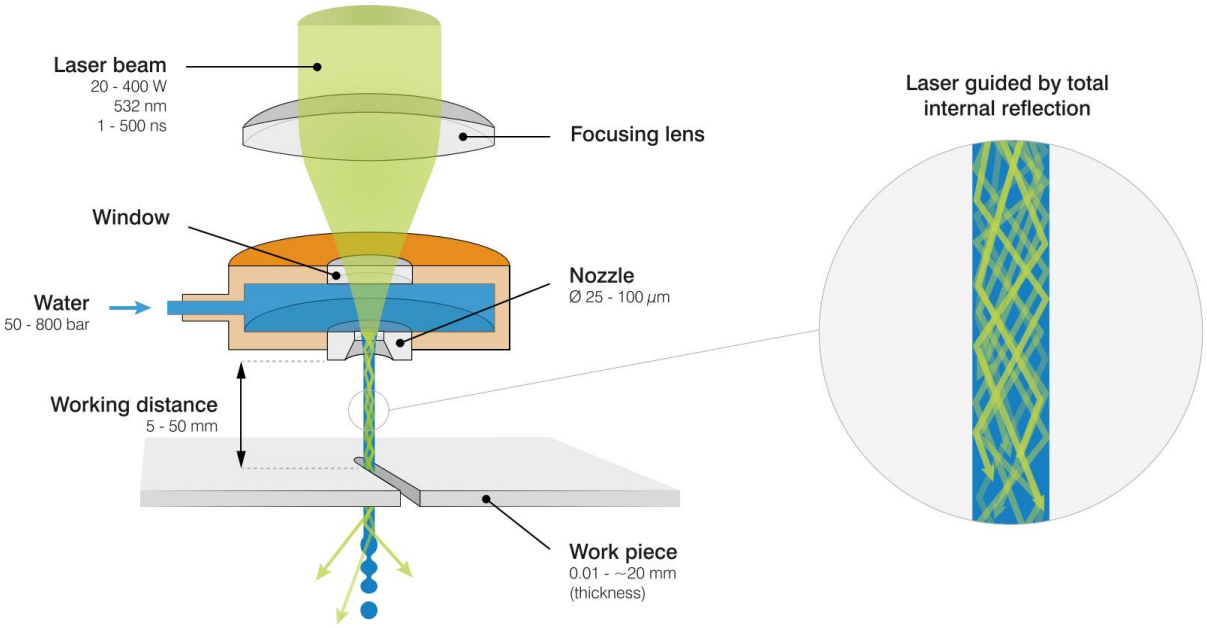

Figure 2.3 Schematic of Synova MicroJet laser set-up[20]

After the samples were produced, scanning electron micrographs were taken using an FEI Teneo low voltage scanning electron microscope at an accelerating voltage of 10.0 kV and a current of 0.40 nA. A back scattered electron (BSE) beam was used to produce higher contrast between the light weight diamond phase and heavier weight silicon carbide phases. These images were then used in a threshold analysis to determine the volume fraction of diamond particles in each sample.

2.2 Laser Flash Analysis (LFA)

Thermal diffusivity (α) is the rate by which a material can absorb heat and is related to the thermal conductivity (k), density (ρ) and specific heat (C_p) seen in the equation below.[23]

$$\alpha = \frac{k}{\rho C_p} \tag{2.2}$$

Laser flash analysis, or LFA, is one method used to measure the thermal diffusivity of a material, in this case the through plane diffusivity. This method uses a laser to emit a flash of energy towards a sample. It is assumed that the front face of the sample absorbs the radiation energy uniformly in that the sample is bounded on the front and back planes by two infinite planes with a finite thickness such that there is one dimensional, axial heat flow through the sample.

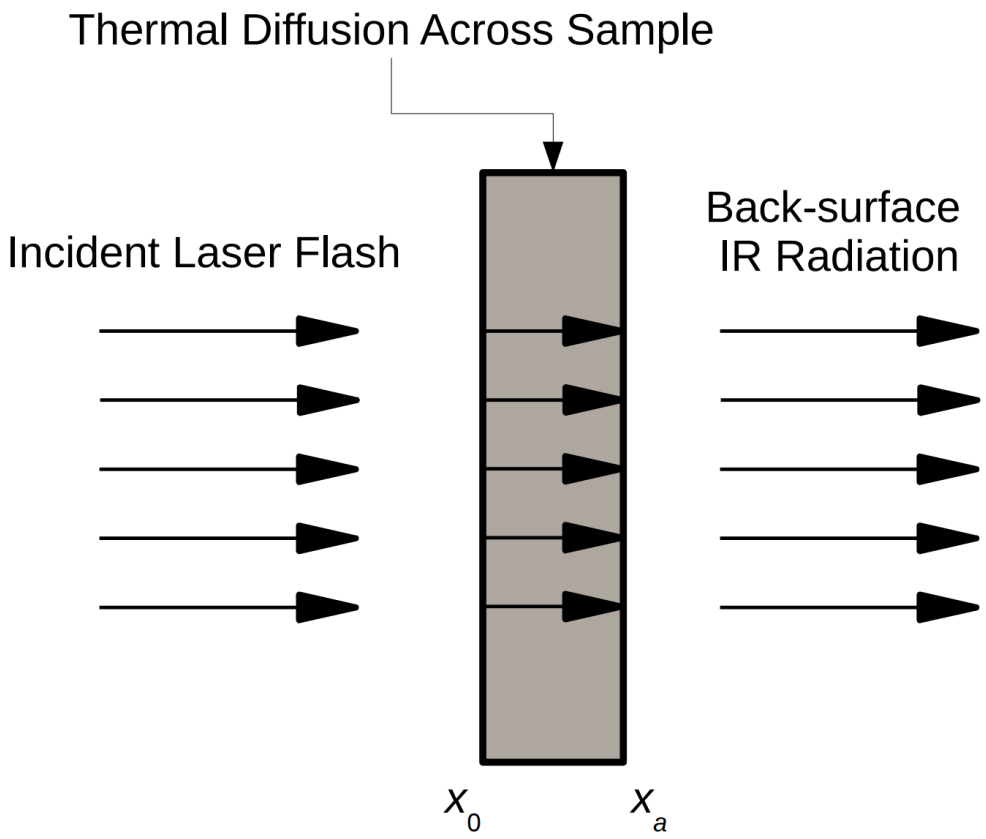

Figure 2.4 One dimensional axial heat flow assumptions used in LFA[24]

The temperature history is recorded such that the temperature (*T*) at the back face of the sample at some time can be expressed by the following equation.

$$T(a,t) = 2T_f \sum_{n=1}^{\infty} \frac{\gamma_n^2(\gamma_n^2 + L^2)\cos\gamma_n}{(\gamma_n^2 - L^2)(\gamma_n^2 + L^2 + 2L)} \exp\left(-\frac{\gamma_n^2 \alpha t}{a^2}\right) \quad 2.3$$

Where T_f is the final adiabatic sample temperature, α is the thermal diffusivity, t is the time required for the heat to travel through the sample, a is the sample thickness and L is the heat loss factor (Biot number).

γ_n is then found by solving the following equation

$$\tan\gamma_n = \frac{2\gamma_n L}{\gamma_n^2 - L^2} \quad 2.4$$

Further assuming that the surface heat losses and radial conduction are negligible, the thermal diffusivity can be calculated using the graph of the recorded temperature history mentioned above such that

$$\alpha = \frac{0.1388a^2}{t_{\frac{1}{2}}} \quad 2.5$$

Where $t_{(1/2)}$ is the time it takes the back surface of the sample to reach half of its maximum temperature. Conversely, Equation 2.5 can also be used to calculate the maximum sample thickness if the diffusivity is known.[23–27]

Specific heat (C_p) can be measured in parallel with thermal diffusivity and is defined as the amount of energy required to increase a unit of mass by one unit of temperature.

$$C_p = \frac{Q}{m\Delta T} \quad 2.6$$

Where Q is the energy, m is the mass and ΔT is the temperature change.

The specific heat of the sample can be comparatively determined through temperature rise curves of the sample and that of a reference sample of known specific heat under the same conditions.[25] In the case of these measurements, the temperature rise was recorded in parallel with the diffusivity measurement. As long as the temperature rise remains small it is proportional to the output voltage change (ΔV) of the infrared detector divided by the amplifier gain (G). Assuming that the flash energy is coupled to the sample in the same way for each sample, the following relationship is derived.[24]

$$Q = apsorbed\ energy = \left(mC_p\Delta T\right)_{reference} = \left(mC_p\Delta T\right)_{sample} \quad 2.7$$

And

$$C_{p_{sample}} = \frac{\left(mC_p\Delta T\right)_{reference}}{\left(mC_p\Delta T\right)_{sample}} = \frac{\left(\left(mC_p\Delta V\right)_{reference}G_{sample}\right)}{(m\Delta V)_{sample}G_{reference}} \quad 2.8$$

Thus, the absorbed energy is a calibration factor for the reference sample that relates mass, specific heat, change in voltage and amplifier gain. The absorbed energy can then be used to calculate the unknown heat capacity of the sample in question. It should also be noted that the change in voltage will be affected by the heat loss factor, L of Equation 2.3. Therefore, the reference sample should have a similar heat loss factor to that of the sample. If this is not the case, then the theoretical voltage change, or final adiabatic temperature, should be used as calculated in Equation 2.3.[24]

The instrument used to measure the thermal diffusivity, heat capacity and thermal conductivity for this experiment was a Netzsch LFA 467 HyperFlash. Standard disk-shaped samples, as prepared by the Synova Laser MicroJet mentioned earlier, with a diameter of 12.7 mm and thickness of 0.5 mm or 5 mm were measured in air at 25˚C. The LFA 467 has a vertical design with a xenon lamp at the bottom as the flash source. The wavelength utilized is in the range of

visible to near IR with a pulse width range of 20 to 1200 µs. The sample then sits between the flash source and the indium antimonide (InSb) or mercury cadmium telluride (MCT) IR detector. See Figure 2.5 for a schematic of the instrument.[24]

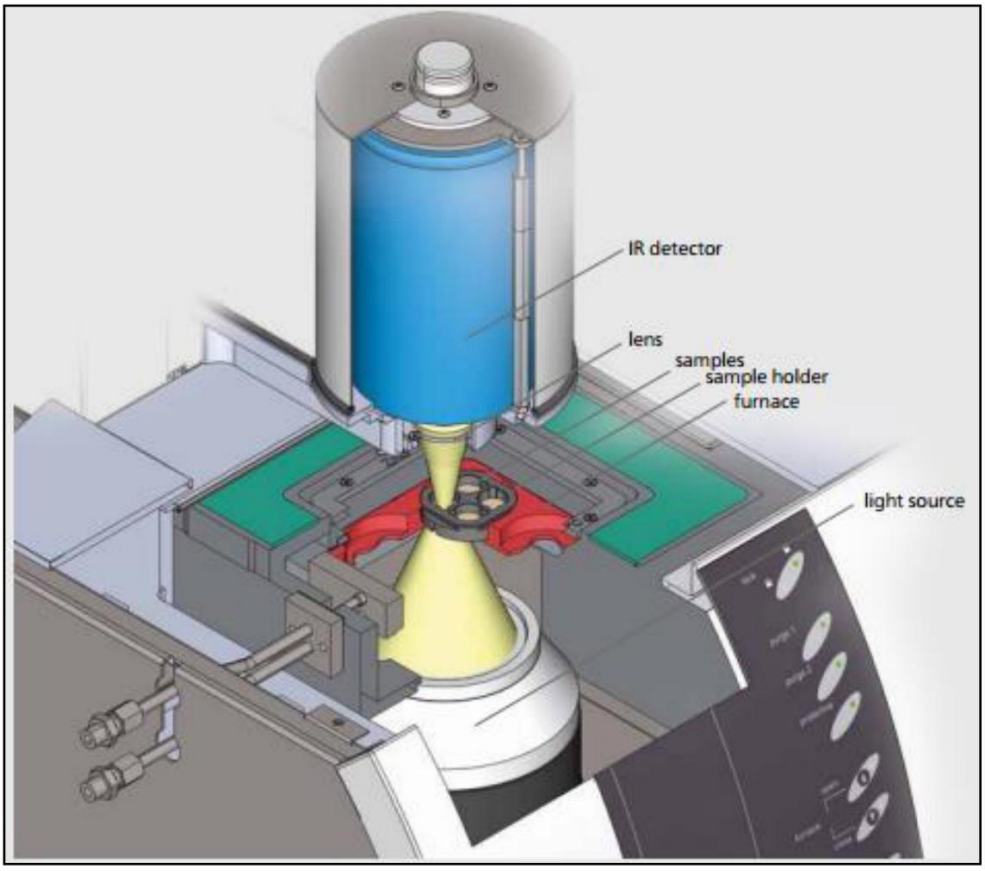

Figure 2.5 Schematic of Netzsch 467 HyperFlash Instrument[24]

When the temperature of the sample is stabilized in the sample chamber, the lamp is fired, and a pulse of energy is absorbed into the front face of the sample. This energy is translated into a temperature rise of 0.5˚C to 2˚C on the back of the sample. The instrument then automatically adjusts the flash lamp charging voltage and pulse width to ensure that the temperature rise is kept within this optimal range. A 2 MHz high speed A/D converter then records and amplifies the temperature rise signal vs. time curve. This process was repeated 10 times per sample over a few

minutes time. The diffusivity and heat capacity were fitted with a best fit curve using the Netzsch 2018 standard fit model.[24]

Absorptivity and transparency of the sample can affect the measurements made by LFA. Due to the transparent nature of both diamond and SiC to some wavelengths of light, special coatings had to be applied to the samples.[7,10,28,29] A layer of graphite approximately 5 μm thick was applied to all of the 5 mm thick samples for diffusivity and heat capacity measurements. The graphite layer is added to increase the absorptivity of the sample, to ensure there is an even absorption over the entire surface area of the sample, and to ensure equal absorptivity over all samples tested.[25] A 5 mm thick Poco graphite sample was used as a reference for the specific heat calibration of the 5 mm thick diamond-SiC samples and therefore also receive the 5 μm thick graphite layer for uniform absorption purposes. It was determined that the thickness of the 5 mm samples was great enough that transmission did not impact these samples. For the 0.5 mm thick samples however, transmission had a significant impact. To combat this issue a 0.2 μm layer of gold was sputter coated onto the samples. A very thin layer of graphite was then applied to the 0.5 mm samples as well, to reduce the reflectivity of the gold layer. A full 0.5 μm coating of graphite was then applied to the 0.5 mm samples for the heat capacity measurements and a 0.5 mm thick sample of high purity copper was used as a reference calibration sample.

2.3 X-Ray Diffraction (XRD)

X – ray diffraction (XRD) is a method of material characterization that uses characteristic x – rays to identify a material compound from its crystal structure. XRD is based on the principles of Bragg's Law dealing with the interference of electromagnetic waves, or x – rays. Two waves traveling in the same direction can interact either constructively or destructively. If constructive interference occurs, then the peaks of one wave are aligned with the peaks of the other and the

amplitude of the wave increases. A phase difference of nλ is produced, where n is an integer, and the waves are said to be in phase. If the peaks of the waves do not line up, destructive interference occurs, and the resulting wave is out of phase. In XRD, incident x – rays are diffracted by the individual crystal planes of the material and the *d* spacing is defined by the distance between each plane of atoms.

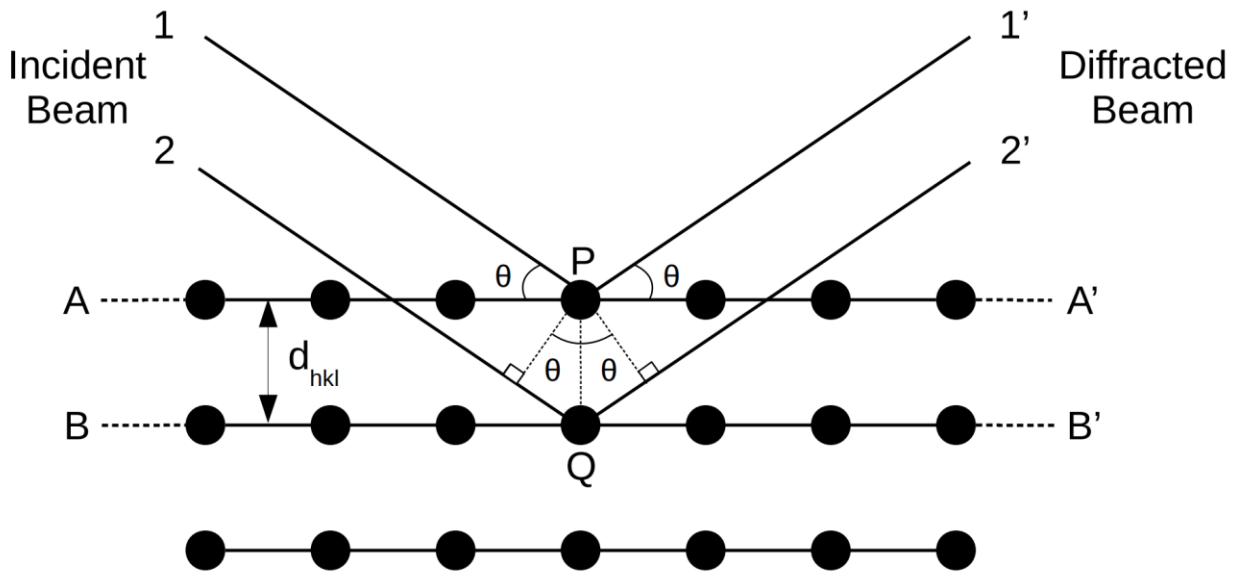

Figure 2.6 Depicts the incident and reflected beam of a Bragg diffracted monoatomic x-ray source interacting constructively through two of atoms with spacing 'd'.[30]

The figure above shows the interaction of incident x – ray beam 1 and 2 on crystal planes *A* and *B* of an unknown material. The deflected planes will only be in phase if Bragg's Law is satisfied:

$$n\lambda = 2d \sin\theta \qquad 2.9$$

Where *n* is an integer, *d* is the spacing between the crystal planes, and θ is the angle of the incident beam. If the spacing between crystal planes in a material is known, the crystal structure can be determined. The spacing, *d*, is determined by:

$$d = \frac{a}{\sqrt{h^2 + k^2 + l^2}} \qquad 2.10$$

where *a* is the lattice parameter, and *(hkl)* represent the miller indices of the crystal. However, before these calculations can be made, the x – rays must first be produced in an x – ray tube, represented in the figure below. An x – ray tube is a device with two electrodes in a vacuum at high voltage that draws electrons from an electron source to an anode, or target.

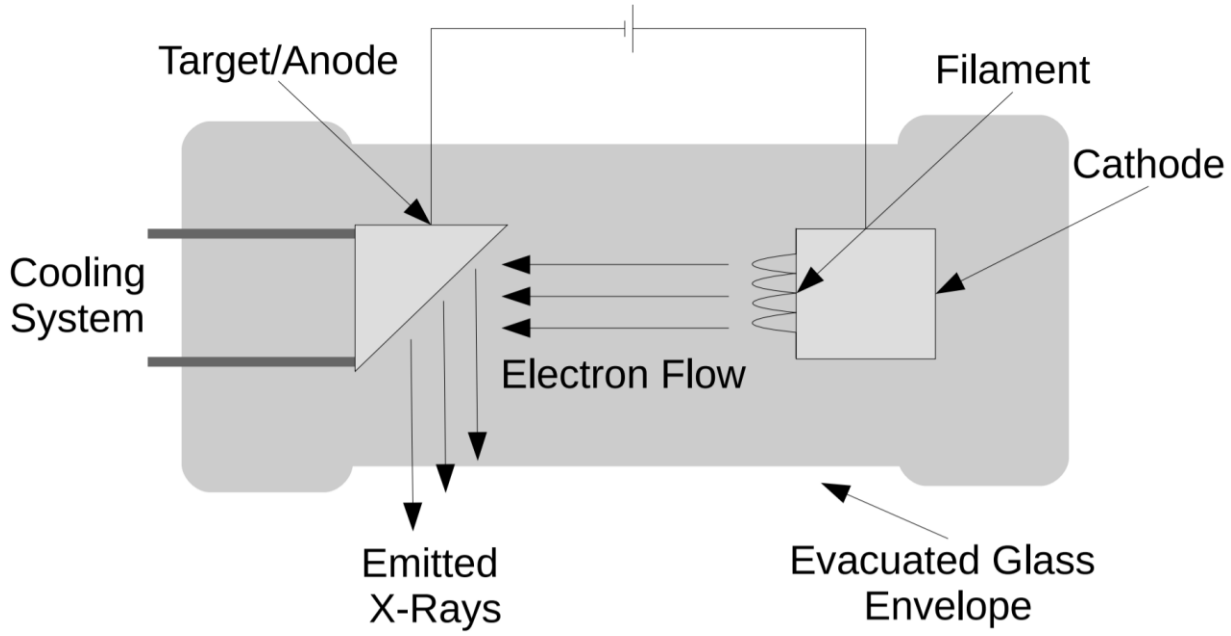

Figure 2.2.7 An x-ray tube used in an x-ray diffractometer to produce an x-ray beam for diffraction.[30]

When the electrons first hit the target, x-rays with a range of wavelengths, known as continuous x – rays, are produced and radiated in all directions. A filter must then be used to gather only the characteristic x – rays, which are those wavelengths that correspond to the sharpest intensity maxima, in order to produce the monochromatic radiation needed for XRD. More specifically, characteristic x – rays are produced when an electron incident to the target in the x – ray tube has enough energy to excite an electron in the inner shell of an atom to a higher energy shell and produce a vacancy. This vacancy is then filled by an electron from an outer shell that

emits a certain wavelength, or characteristic x – ray, when falling to the lower energy level. For example, as seen in the figure below, if a K shell electron is excited to a higher energy state, Kα x – rays are produced if the electron that fills the vacancy falls from the L shell, while Kβ x – rays are produced if the vacancy is filled by an electron from the M shell.

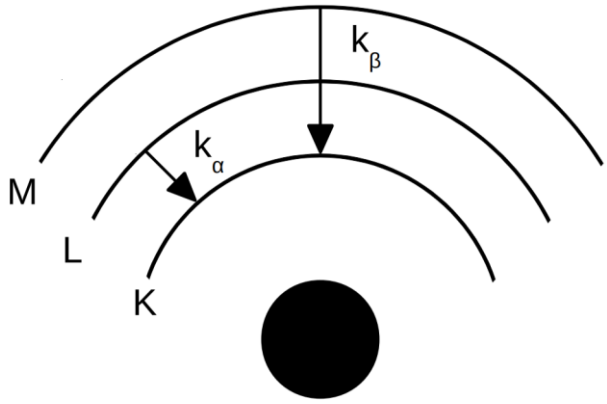

Figure 2.8 Schematic of x - ray radiation.[30]

Furthermore, since the probability of an electron falling from the L shell to fill the K shell vacancy is much higher than the probability of an electron falling from the M shell, the intensity of the Kα x – rays is greater than the resulting intensity from the Kβ x – rays. The filter is able to obtain monochromatic Kα x – rays when it is made from a material that absorbs continuous and Kβ x – rays, or x – rays with smaller wavelength than that of Kα. The intensity (I) of an x – ray that passes through the absorption layer of the filter with a thickness, *x*, can be determined by:

$$I_x = I_o e^{\left(\frac{\mu}{\rho}\right)\rho x} \qquad 2.11$$

Where (μ/ρ) is the linear absorption coefficient divided by the density of the material, known as the mass absorption coefficient. The mass absorption coefficient is determined by chemical element.

Before the final diffraction pattern can be determined the x – rays must pass through a number of other components. The figure below shows a schematic of a typical set up of an x – ray diffractometer.

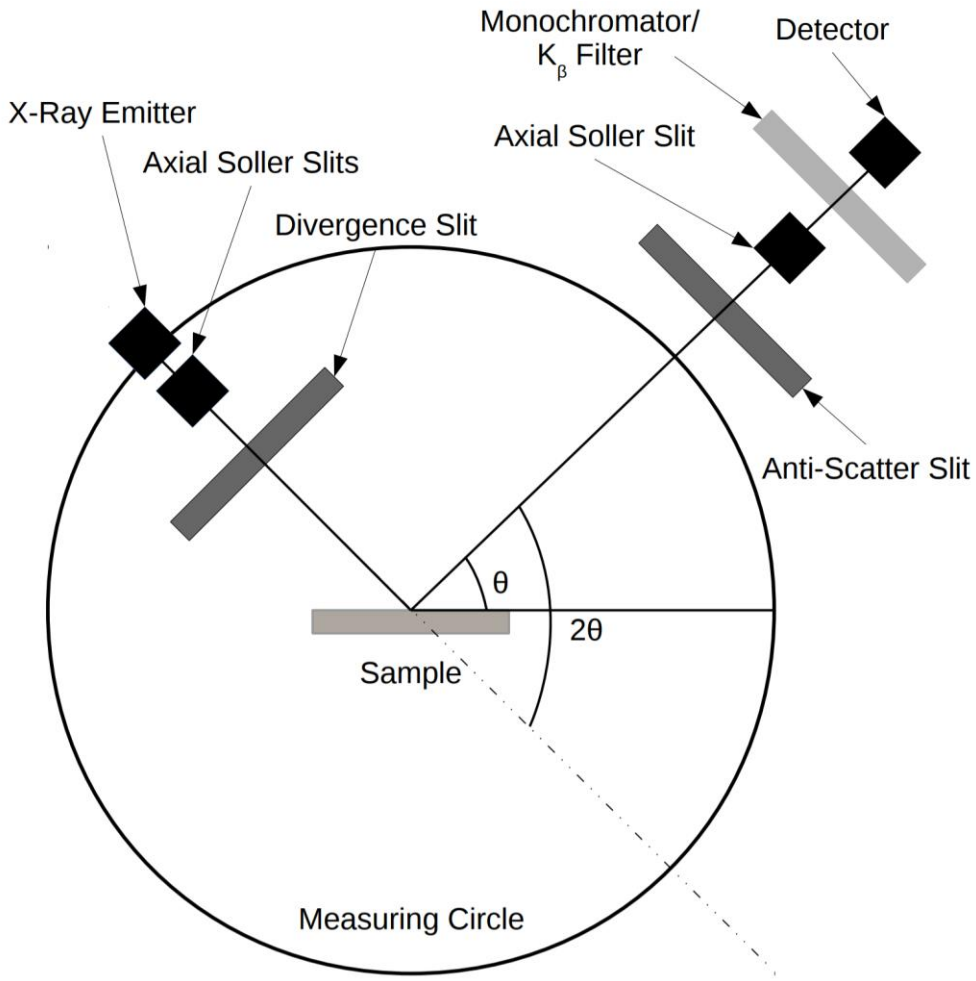

Figure 2.9 Geometric configuration of an x-ray diffractometer.[30]

After the x-rays are produced in the x-ray tube on the left, they pass through Soller slits. Soller slits are comprised of a series of metal plates oriented parallel to the figure plane with the purpose of preventing perpendicular divergence of the x-rays in that plane. The divergent x-rays that pass through the Soller slits strike the sample and then converge in the receiving, or axial Sollar slit. From here, the x-rays enter the monochromatic filter, known as a monochromator, before passing to the detector the monochromator serves to reduce the background noise from the

sample while also damping wavelengths other than Kα. To ensure that a 2θ diffraction intensity range is measured, the Bragg-Brentano arrangement is typically used. In this arrangement, both the detector and receiving slits rotate along the axis of the measuring circle at twice the speed of the rotation of the sample, while the x-ray source is fixed.[30]

For the case examined here, a Bruker Phaser D2 x-ray diffractometer was used at a voltage of 30 kV and a current of 10 mA. A copper source with a Cu-Kα wavelength of 1.540562 (Å), Cu-Kβ wavelength of 1.392218 (Å) and step size of 0.2 s was used to evaluate the samples over a two-theta range of 20˚ to 135˚.[31] Vesta 3 Series software and Match! Phase Identification Software version 3.7.0.124 were used to narrow down possible peak matches.[32,33]

Chapter 3 Results and Discussion

According to Callister, "…a composite is considered to be any multiphase material that exhibits a significant proportion of the properties of both constituent phases such that a better combination of properties is realized." A composite is generally comprised of a matrix phase, or continuous phase which encircles the dispersed phase. The properties of the composite are related to both the matrix and the dispersed phase but are largely influenced by the geometry of the dispersed phase. Such geometric factors include particle shape, size, orientation and distribution in the matrix.[34] In the ideal case examined here, SiC is the matrix phase encompassing the dispersed diamond particles.

3.1 SEM Micrographs

A scanning electron microscope (SEM) was used to take micrographs of all eight samples at 1000x as seen in the figures below. A back scattered electron beam was used for these images therefore the darker areas can be assumed to represent lower atomic weight elements.[30] Thus, the diamonds are represented by the dark grains surrounded by a lighter color matrix of Si and multiple polymorphs of SiC, discussed in the following section. Furthermore, the volume fraction of dispersed diamond particles in the matrix was determined by threshold analysis of scanning electron micrographs of ten different locations per sample. The results of the analysis are below. It should be noted that volume fraction increases as the diameter of the diamond particles increases.

Table 3.1 Shows the volume fraction of diamond as related to sample name and diamond particle size.

Sample Name	Average Particle Size (um)	Volume Fraction
A	22	0.33
B	45	0.42
C	65	0.53
D	100	0.53
E	150	0.59
F	212	0.58
G	355	0.66
H	500	0.72

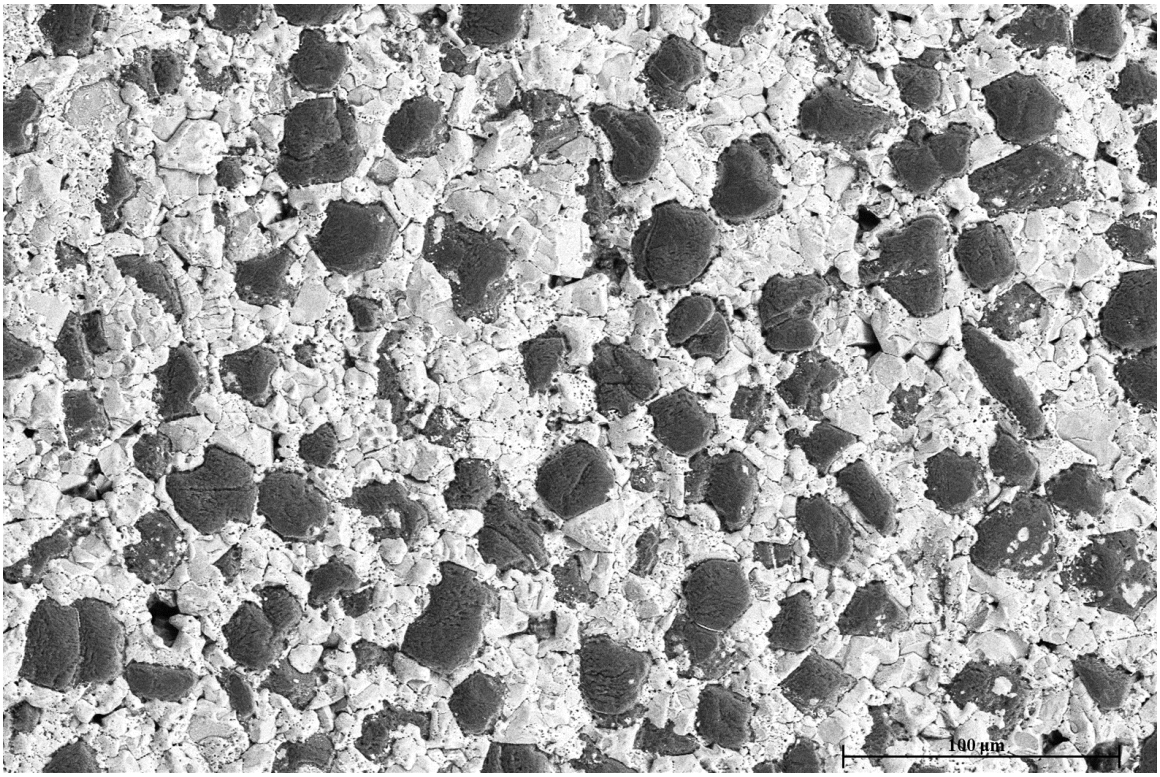

Figure 3.1 SEM back scattered image of Sample A, 22 µm diamond particles, at 1000x magnification.

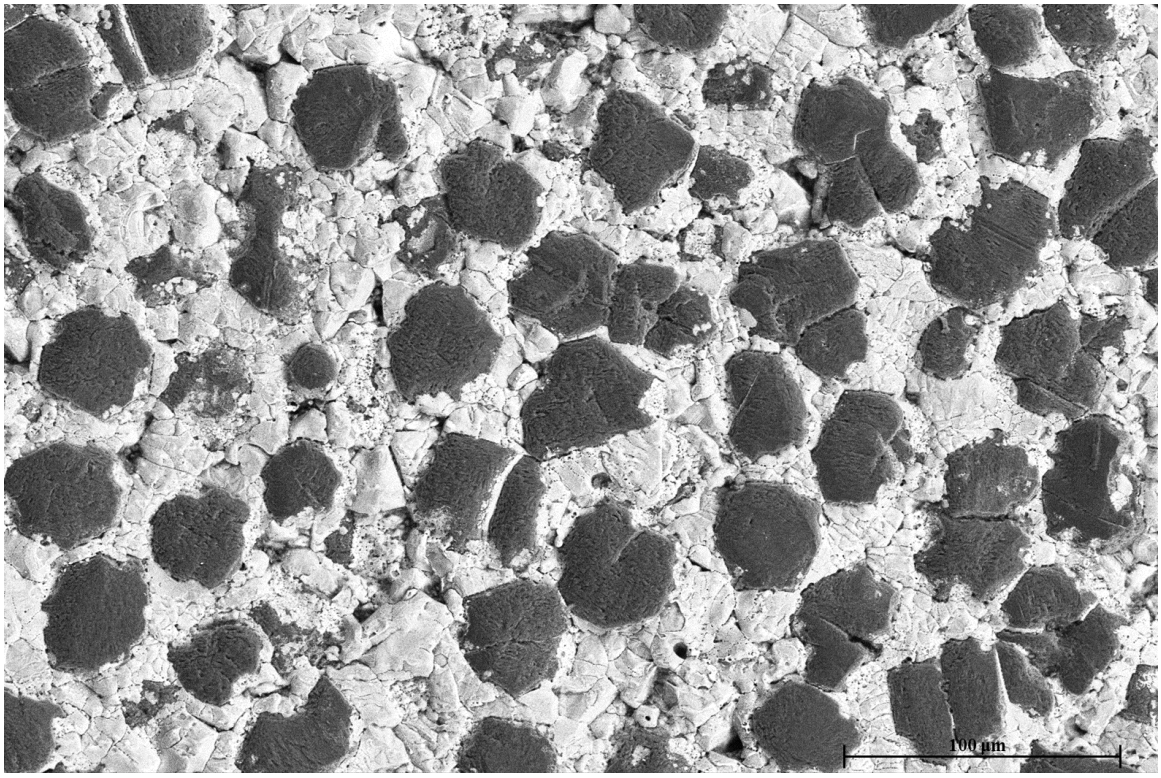

Figure 3.2 SEM back scattered image of Sample B, 45 µm diamond particles, at 1000x magnification.

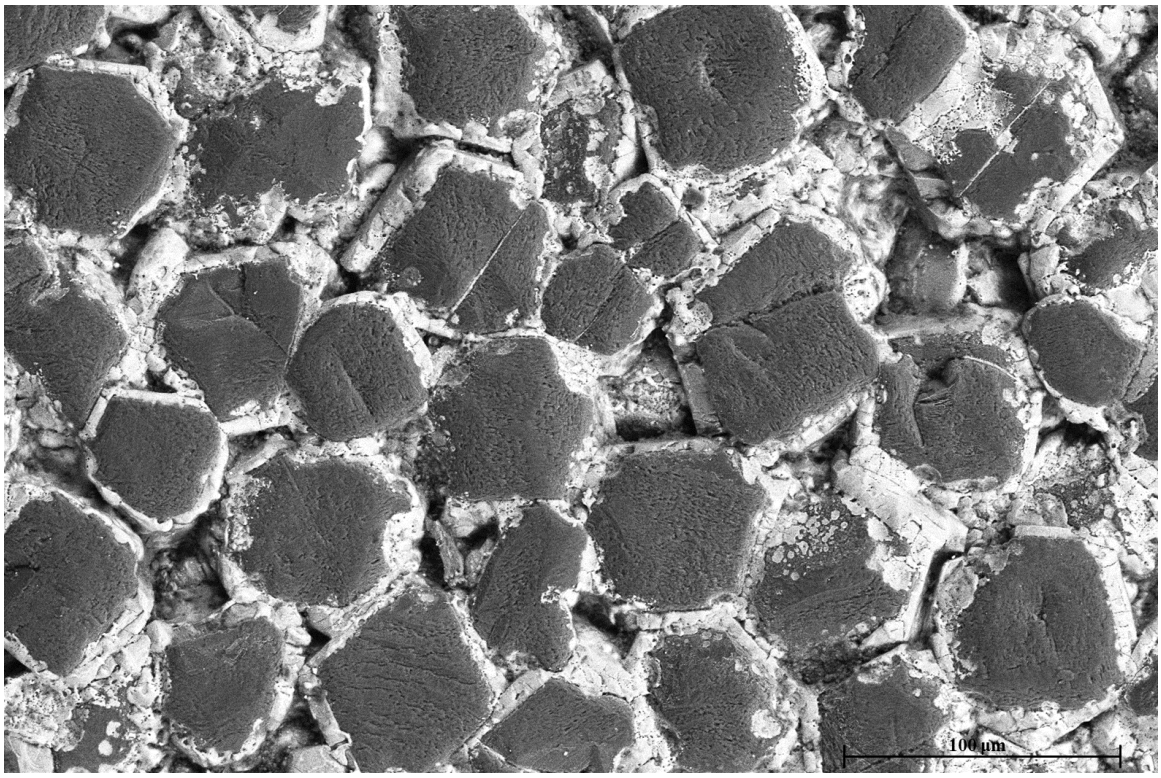

Figure 3.3 SEM back scattered image of Sample C, 65 µm diamond particles, at 1000x magnification.

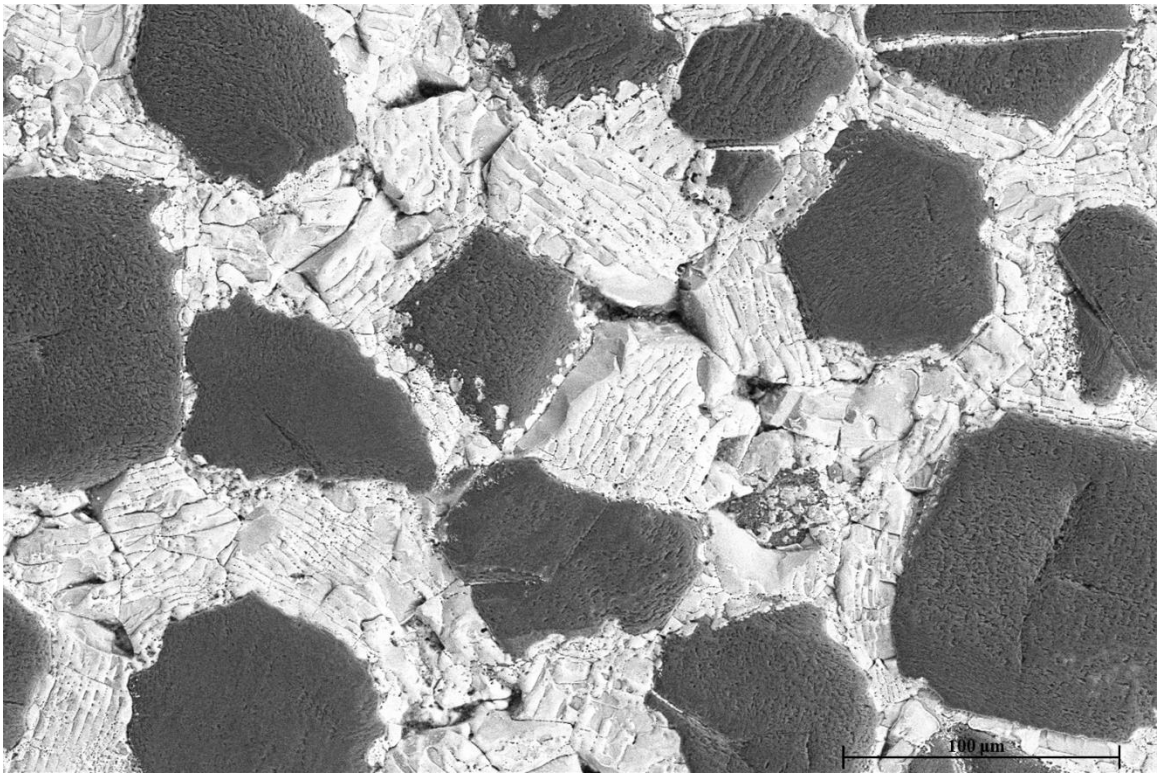

Figure 3.4 SEM back scattered image of Sample D, 100 µm diamond particles, at 1000x magnification.

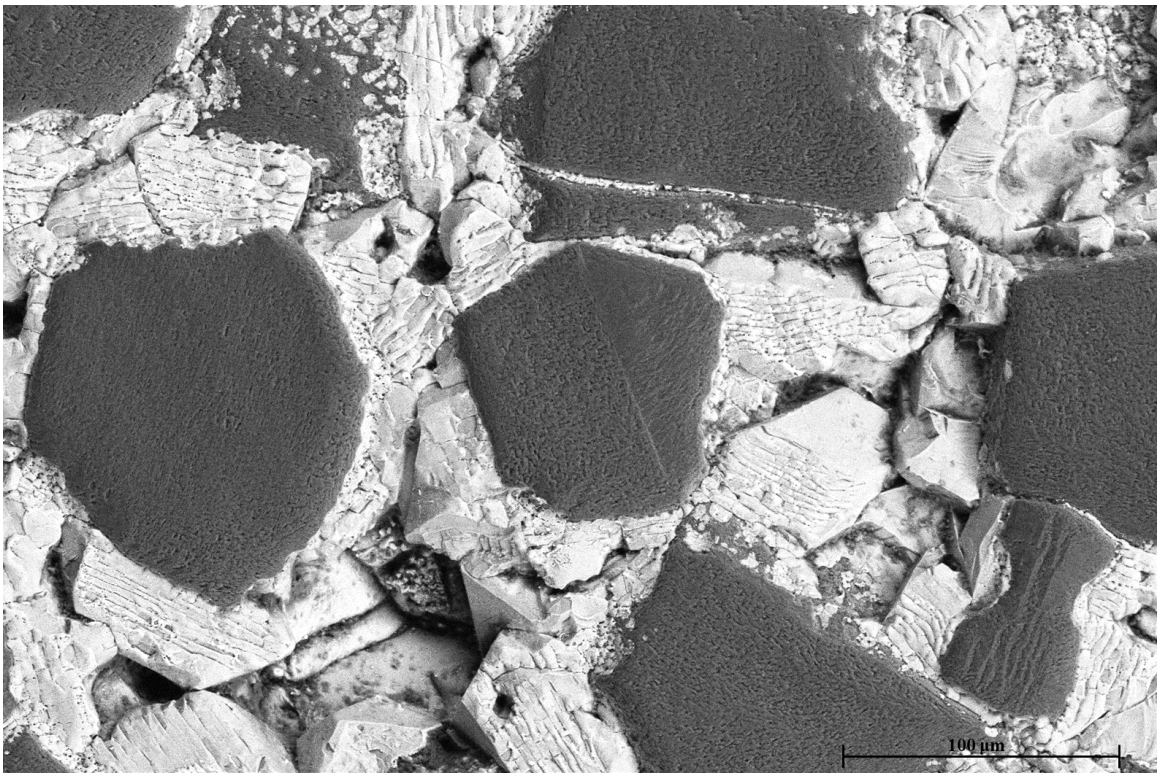

Figure 3.5 SEM back scattered image of Sample E, 150 µm diamond particles, at 1000x magnification.

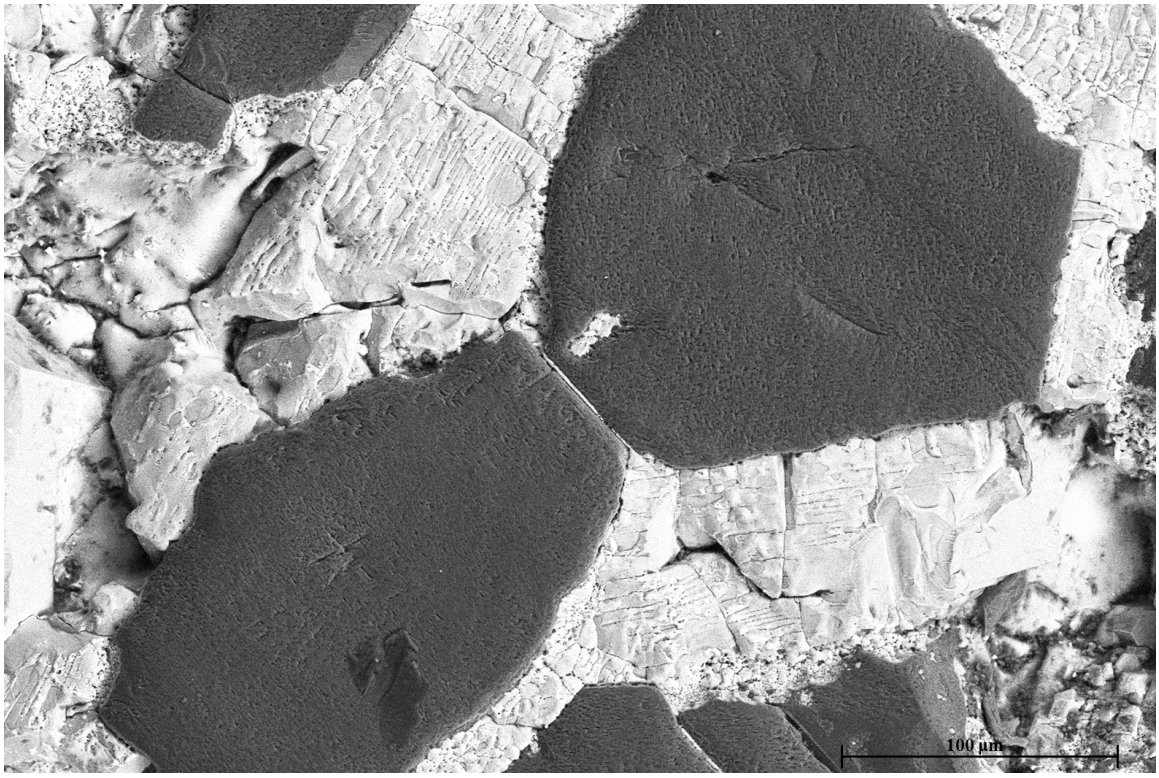

Figure 3.6 SEM back scattered image of Sample F, 212 µm diamond particles, at 1000x magnification.

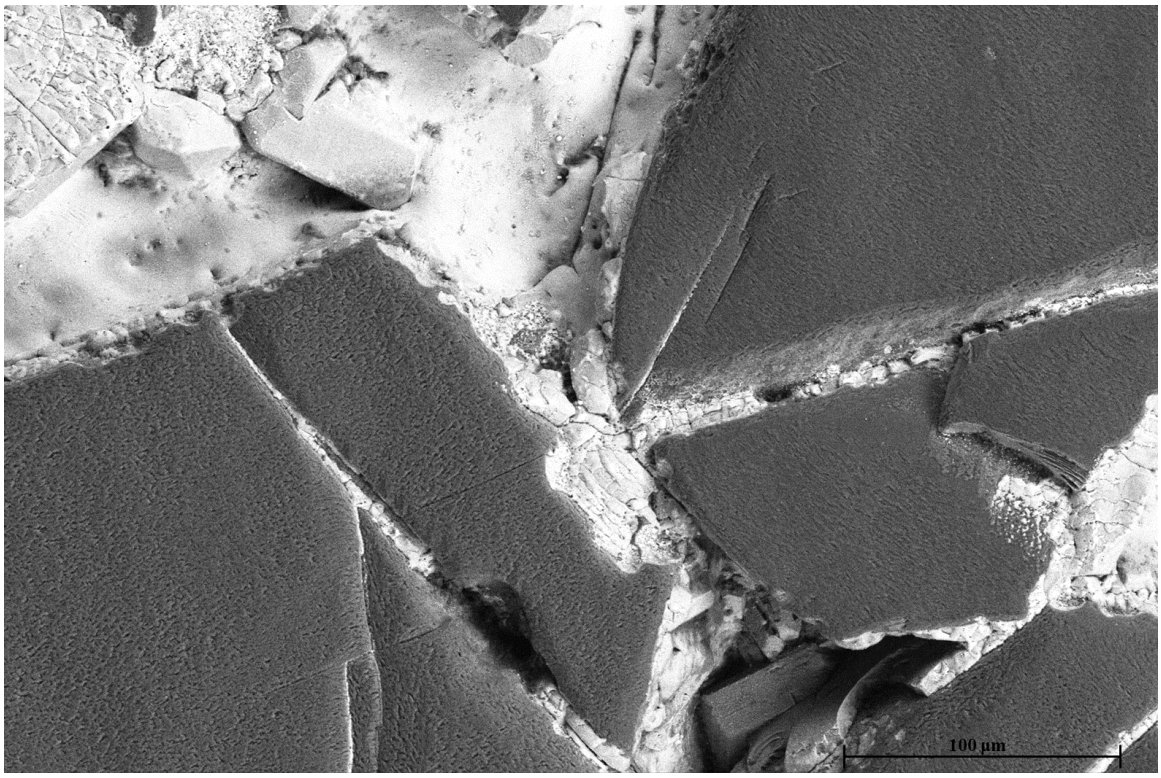

Figure 3.7 SEM back scattered image of Sample G, 355 µm diamond particles, at 1000x magnification.

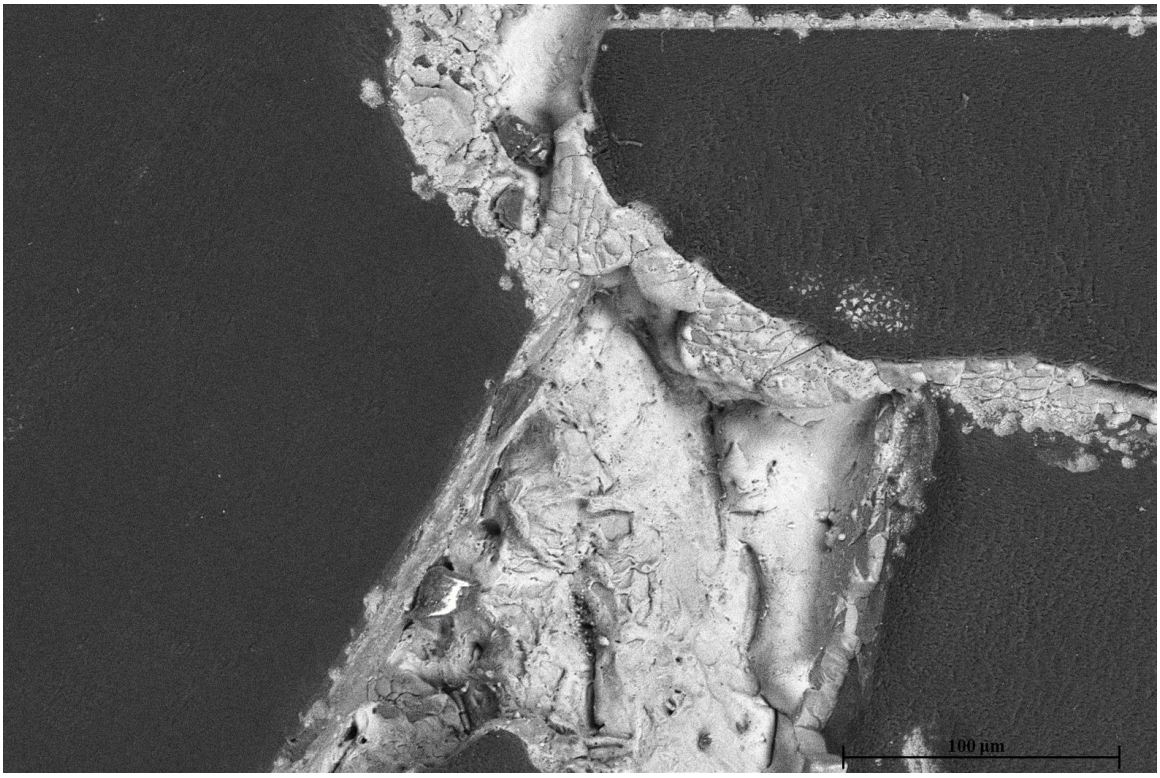

Figure 3.8 SEM back scattered image of Sample H, 500 µm diamond particles, at 1000x magnification.

Upon inspection, the silicon-carbon reaction can be seen forming a clear perimeter of SiC around each of the diamond grains. At higher magnification, it is also possible to see epitaxial growth of SiC on the diamond grains, shown below as the lines emanating perpendicular to each of the diamond faces.

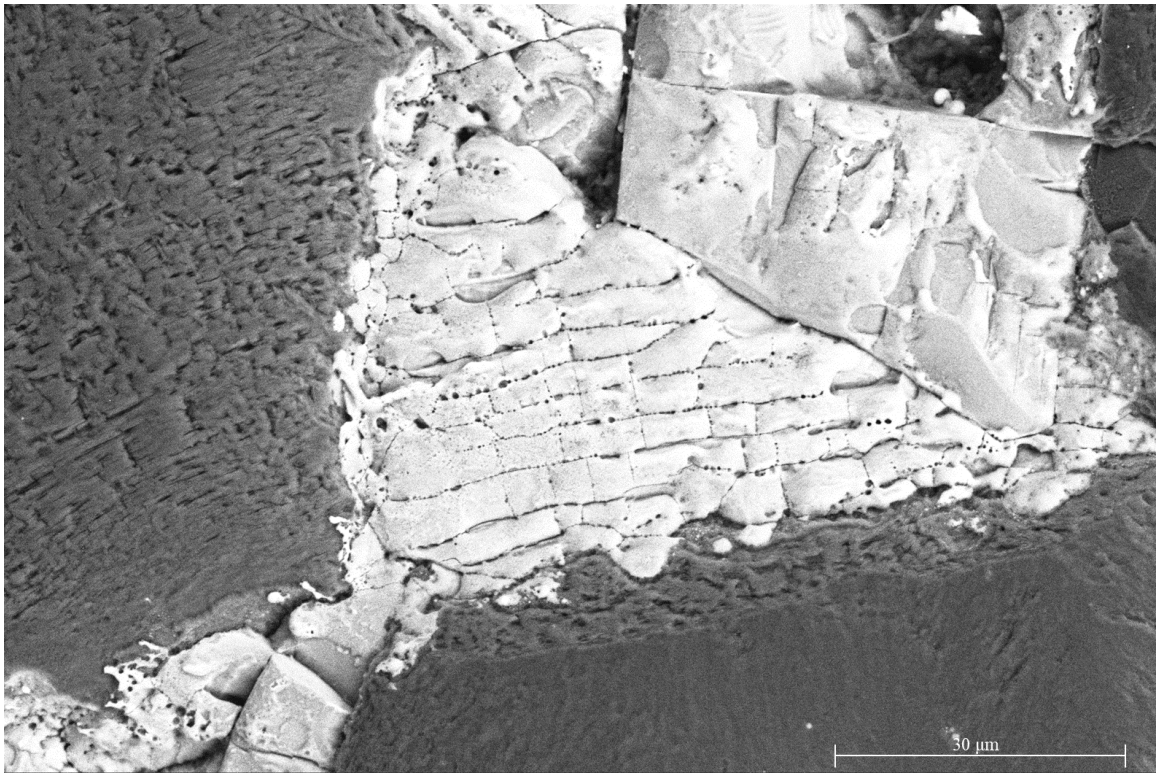

Figure 3.9 Example of epitaxial growth of SiC on diamond grains as seen in Sample D (100 µm) at 3500x magnification.

Several defects can be seen in these images, but perhaps the most noticeable defect are the pores in each sample. The pores tend to form between the boundaries of the reacted SiC layer and are most noticeable in sample C (65 µm). Liquid silicon is known to infiltrate preforms from the faces of the preform before penetrating the center. Due to this infiltration direction, the silicon reacts with the carbon along the edges of the sample first and has been known to produce a choking off effect towards the center of the sample such that so much SiC is formed around the edges of the sample that the Si is prevented from penetrating the center. However, this effect is usually seen at small particle sizes of diamond suggesting that other effects may be causing the pores seen here.[35,36] Another defect seen in these micrographs is cracking throughout the microstructure. Liquid silicon infiltration is known to produce cracking due to the expansion of SiC during the silicon-carbon reaction, however it is not possible to adequately determine if these microcracks are due to SiC formation or from subsequent laser processing.[35]

3.2 X-Ray Diffraction

X-ray diffraction (XRD) was used to determine the crystalline phases present in the eight diamond-SiC samples. The XRD spectrums and correlating plane matching is shown at the end of this section. Results of this analysis can be split up by sample group. Samples A, B and C, or 22 μm, 45 μm and 65 μm respectively all had Cu-Kα peaks from cubic 3C-SiC, diamond, silicon, and gold. Cu-kβ peaks of the 3C-SiC and diamond were observed at (111) in each material. Samples D-H, or 100 μm to 500 μm, exhibit the peaks of all the above mentioned phases as well as those of hexagonal 6H-SiC and rhombohedral 51R-SiC. These larger particle size samples also have additional Cu-kβ diffraction peaks at (220) and (311) in diamond and at (101) in 6H-Sic. Additional information regarding each phase and its corresponding space group and lattice parameters is seen in the table below. As per naming convention, β-SiC is comprised only of the 3C-SiC polymorph while α-SiC is used to describe all other SiC polymorphs.[37]

Table 3.2 Phases identified by XRD for diamond-SiC and their corresponding crystallographic parameters.

Phase	Space Group	Lattice Parameter, a (Å)	Lattice Parameter, b (Å)	Lattice Parameter, c (Å)	α (degrees)	β (degrees)	ϒ (degrees)	Reference
β-SiC	F-43m	4.348	4.348	4.348	90	90	90	[38]
Diamond	Fd-3m:1	3.567	3.567	3.567	90	90	90	[39]
Silicon	Fd-3m:1	5.4304	5.4304	5.4304	90	90	90	[40]
Gold	Fm-3m	4.134	4.134	4.134	90	90	90	[41]
α-SiC, 6H	P63	3.095	3.095	15.17	90	90	120	[42]
α-SiC, 51R	R3mH	3.073	3.073	128.15	90	90	120	[43]

The processing parameters used to infiltrate these samples with liquid silicon were designed to maximize the formation of the SiC matrix. Ideally, the reaction would go to completion and the silicon phase would be absent. Thus, it is expected that XRD characterization should yield a SiC phase and a diamond phase. The presence of a silicon phase in all samples indicates that not all silicon was reacted into SiC during infiltration. Further investigation into processing parameters

is required to optimize this transformation. The presence of low intensity gold peaks is not unexpected due to the order of measurement operations. Due to available XRD sample holders, the 0.5 mm thick samples were used for XRD analysis. Unfortunately, the analysis was performed after the thermal conductivity measurements were taken which required all of the 0.5 mm samples to be sputter coated in gold, as mentioned previously in the methods section. The samples were ground to remove the gold before XRD characterization, however residual gold remained in the pours of the sample, thus resulting in the presence of low intensity gold peaks. The figure below is the 0.5 mm thick 45 μm sample B. A backscattered electron detector was used to capture this SEM image and further EDS analysis confirmed that the bright areas seen in this sample are gold.

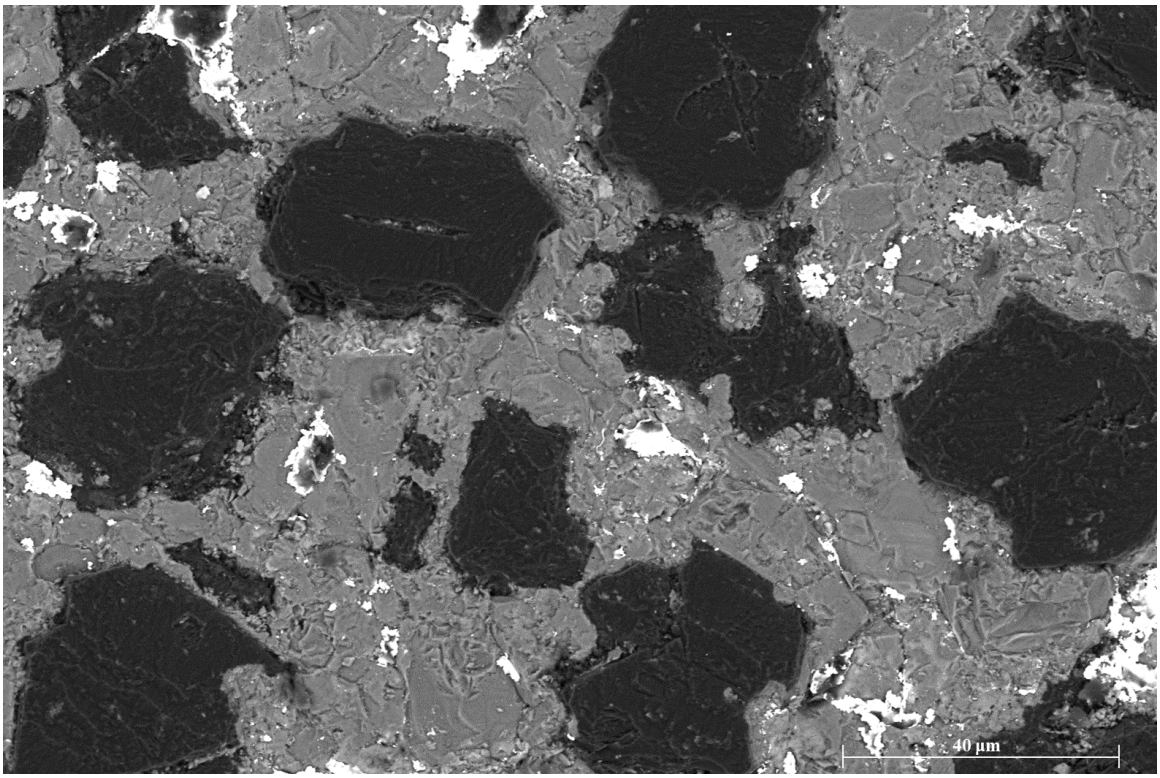

Figure 3.10 SEM image taken with a backscatter electron detector of a 45 μm diamond sample. The bright areas correspond to residual gold stuck in the pores of the sample from LFA analysis.

While there are many polymorphs of SiC, the presence of three different polymorphs in the majority of samples is intriguing, especially as all samples were processed under the same conditions in the same infiltration run. The presence of both 3C β-SiC and 6H α-SiC has been

shown by Salamone in other work with liquid silicon infiltration of diamond-SiC materials under similar processing parameters.[44] Symmetry of α-SiC is similar for all polymorphs such that all atoms lie on the same symmetry axis in the $(11\bar{2}0)$ plane. Furthermore, all α-SiC polymorphs are comprised of identical layers of atoms. The only difference between the polymorphs is the direction of stacking of each plane and the number of planes stacked in each direction before changing directions. This can make phase analysis complex.[37] This is especially applicable to 6H-SiC and 51R-SiC formed here. There are multiple peaks which overlap in the XRD data with similar intensities. Thus, Rietveld analysis is needed to confirm the presence of both 6H-SiC and 51R-SiC and determine the quantity of each.

While samples G and H both exhibit peaks of all three polymorphs of SiC, they differ from the rest of the samples. Sample G, 355 μm, has its most intense peak reflected at (111) in silicon. The most intense peaks of all the other samples correspond to either diamond or one of the polymorphs of SiC. Peak intensity is not directly related to the amount of that phase present in the material, thus, one cannot conclude that the majority phase in sample G is silicon.[30] Furthermore, the volume fraction of 66% diamond particles negates this possibility. Another explanation may be preferential silicon grain growth on certain faces of diamond thus creating a texture and explaining the high intensity. Texture is also seen in sample H in regard to the diamond (311) peak. In theory, the most intense peak of diamond should lie at the (111) reflection.[39] One likely explanation for this texture, or preferential orientation with respect to (311) is the 1 mm by 20 mm spot size of the XRD machine. Sample H is comprised of 500 μm diameter diamond particles, is only 12.7 mm in diameter and has a volume fraction of 72% diamond. Though the distribution of diamonds is random in this sample, the size and volume fraction of diamond particles is so great that it is unlikely that the distribution remained random over the small beam area as is often the

case in samples of large particle size or course powders.[30] To verify this assumption, further XRD testing should be performed where the sample is rotated between measurements, as each rotation has the possibility to yield a different preferred orientation. It is possible that these rotations would produce results yielding the most intense diamond peak at (111). Additionally, measuring the raw 500 μm diamond powder would provide a helpful baseline to compare to the apparent texture seen in results from Sample H. Preferred orientation could also result from preferential stacking of well-defined diamond crystallites during sample preparation, or be a result of initial processing parameters in diamond formation. For example, Tang et al. found that additions of oxygen and/or nitrogen during CVD diamond formation can cause preferential growth.[45]

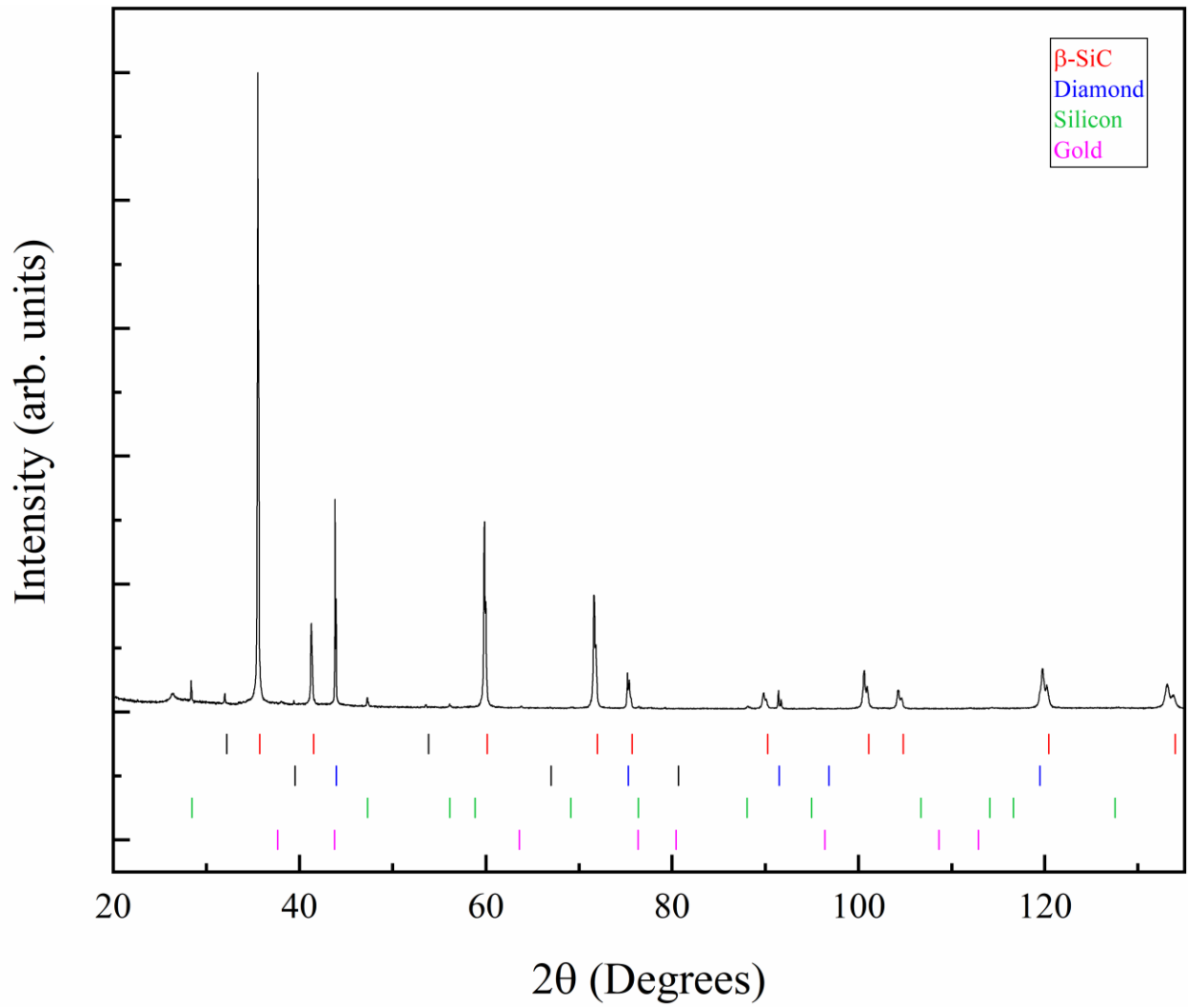

Figure 3.11 X-ray diffraction pattern of Sample A, 22 μm diamond particles. The black lines denote Cu-kβ peaks.

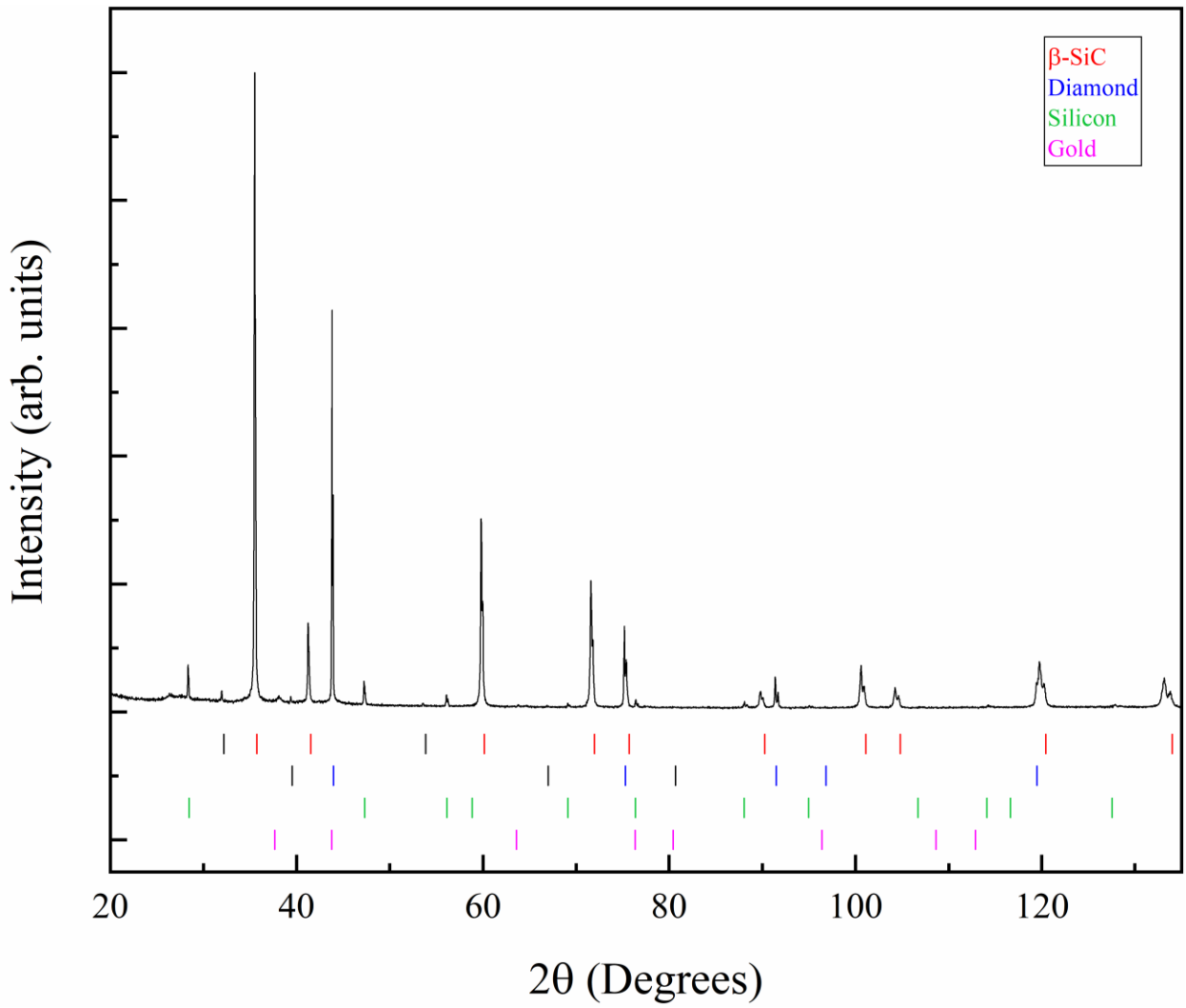

Figure 3.12 X-ray diffraction pattern of Sample B, 45 μm diamond particles. The black lines denote Cu-kβ peaks.

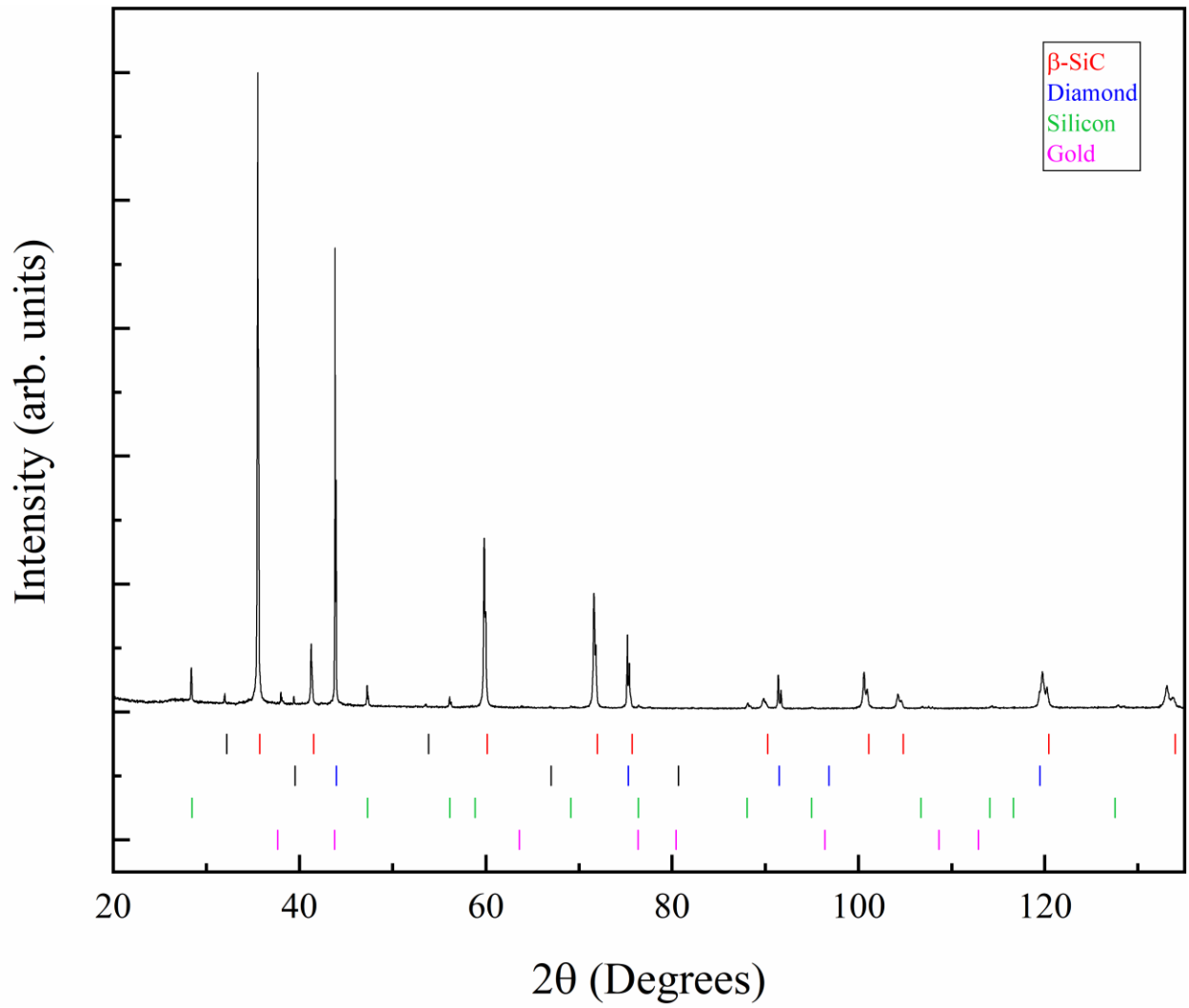

Figure 3.13 X-ray diffraction pattern of Sample C, 65 μm diamond particles. The black lines denote Cu-kβ peaks.

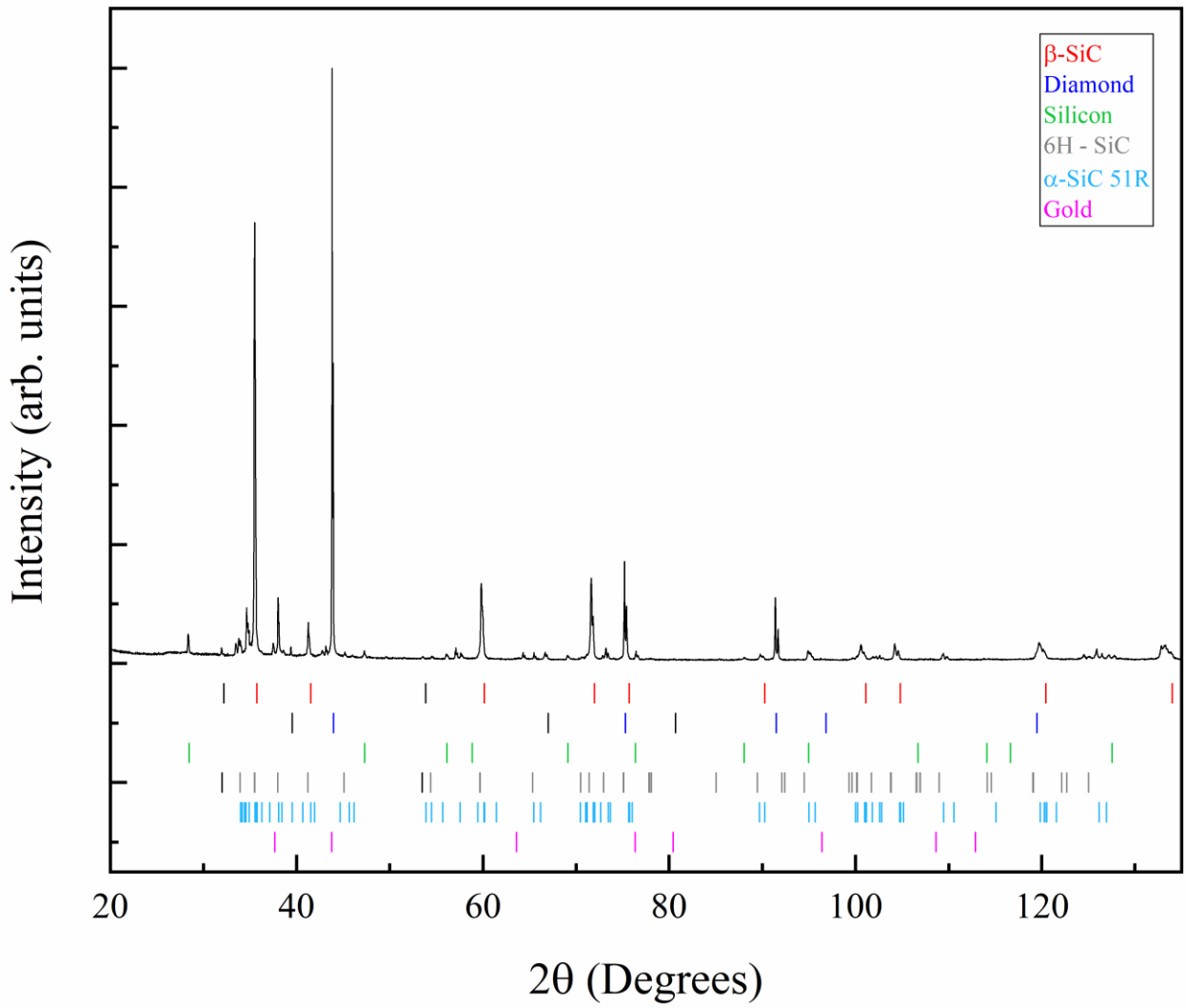

Figure 3.14 X-ray diffraction pattern of Sample D, 100 μm diamond particles. The black lines denote Cu-kβ peaks.

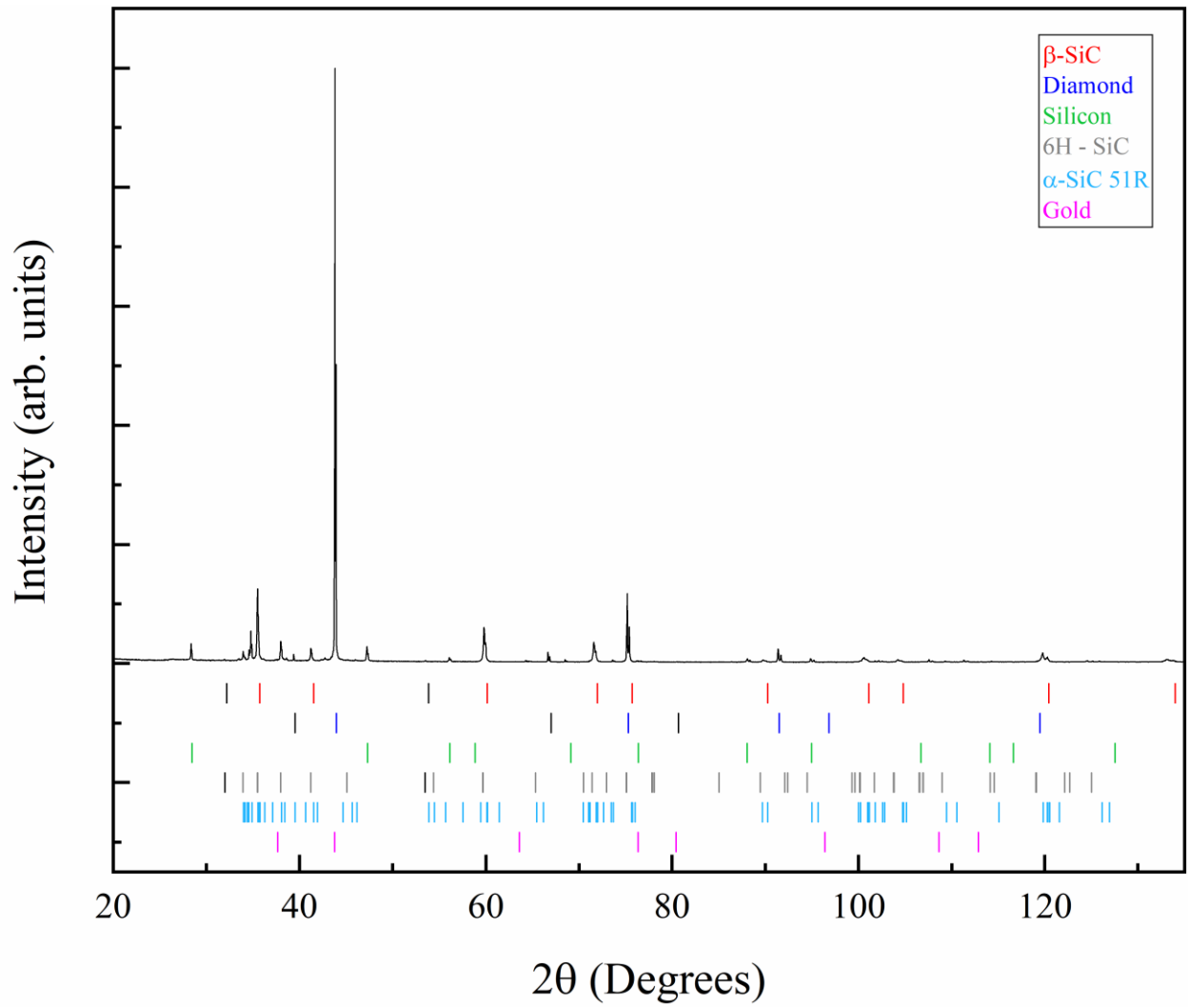

Figure 3.15 X-ray diffraction pattern of Sample E, 150 μm diamond particles. The black lines denote Cu-kβ peaks.

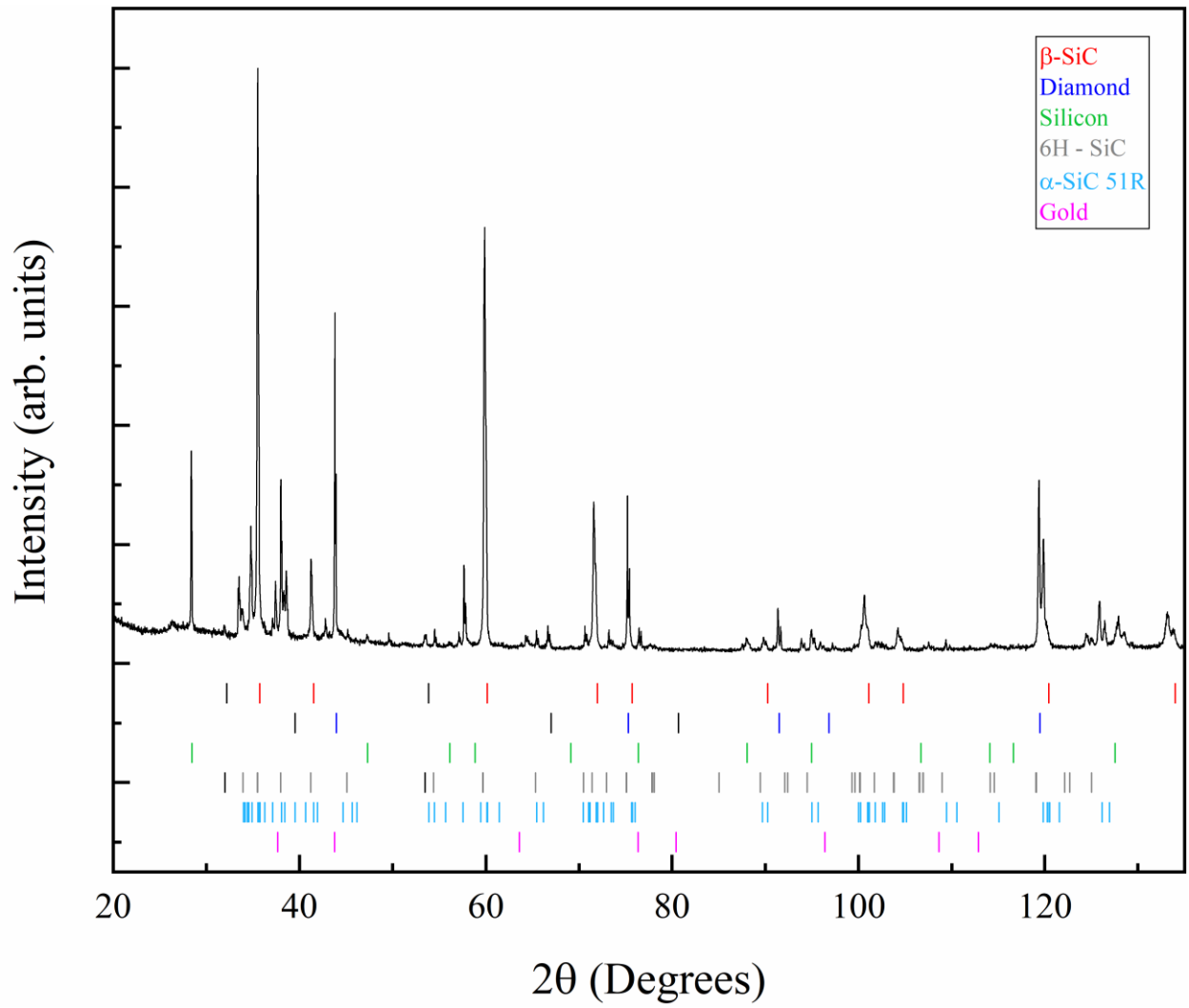

Figure 3.16 X-ray diffraction pattern of Sample F, 212 μm diamond particles. The black lines denote Cu-kβ peaks.

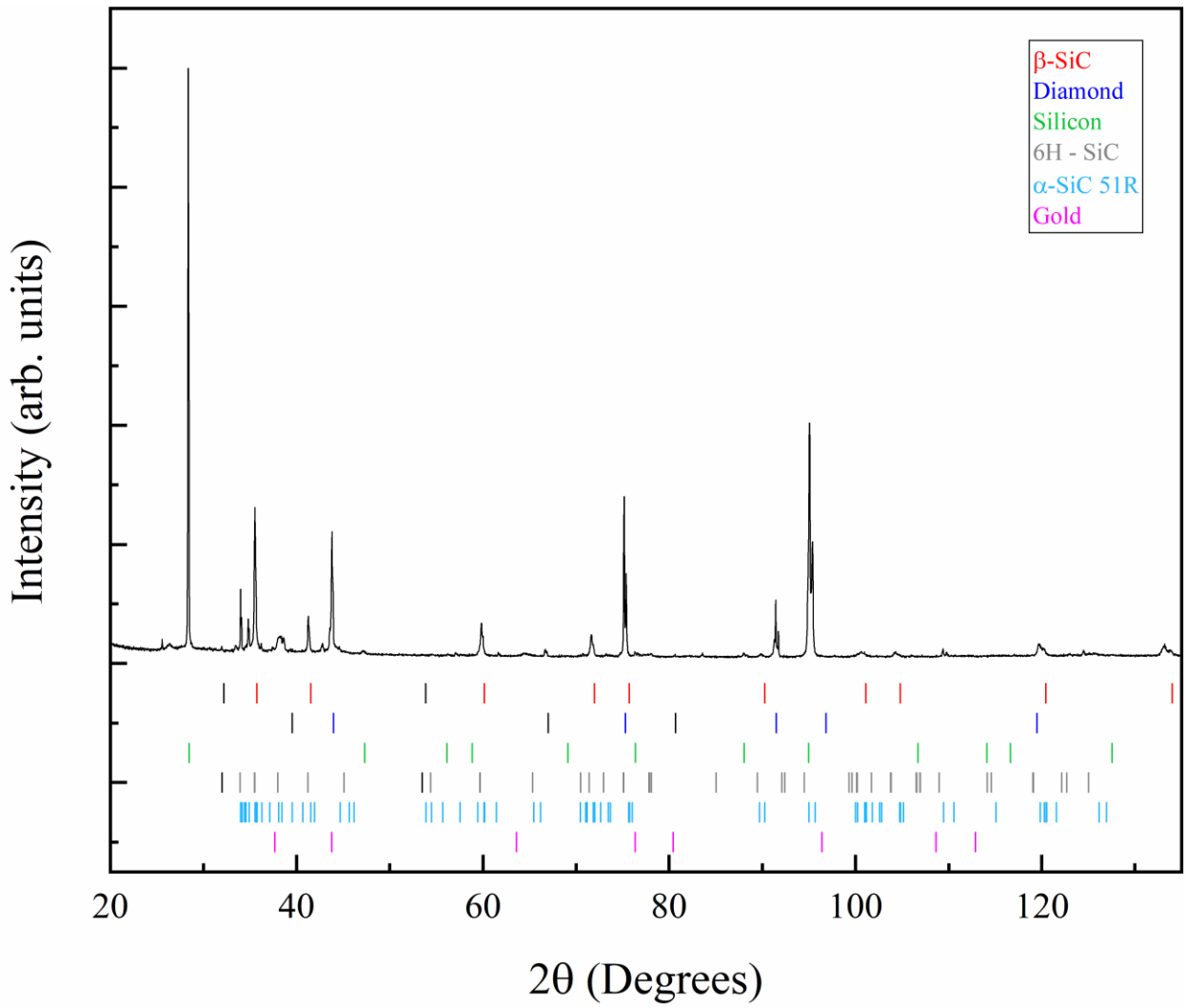

Figure 3.17 X-ray diffraction pattern of Sample G, 355 μm diamond particles. The black lines denote Cu-kβ peaks.

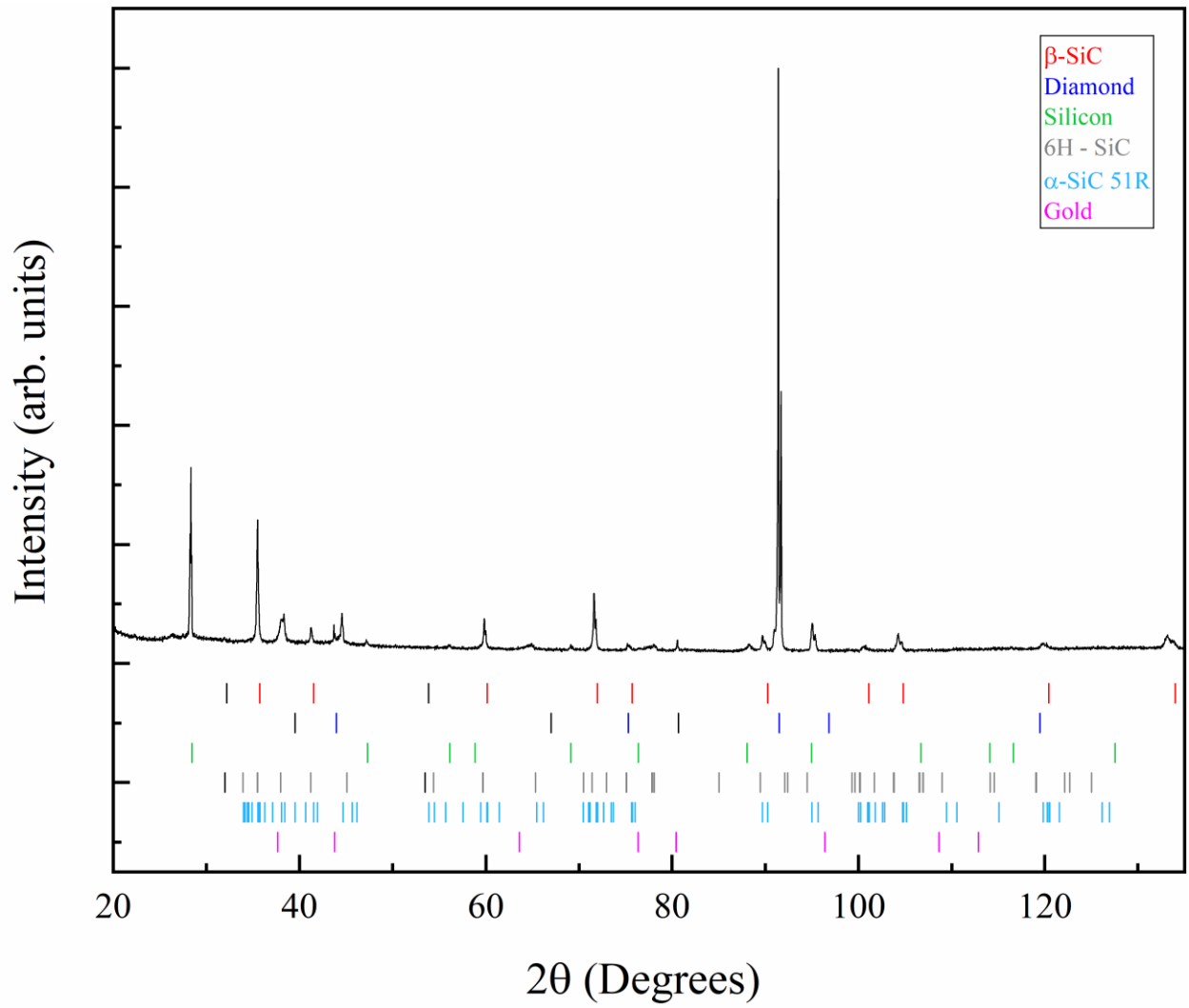

Figure 3.18 X-ray diffraction pattern of Sample H, 500 μm diamond particles. The black lines denote Cu-kβ peaks.

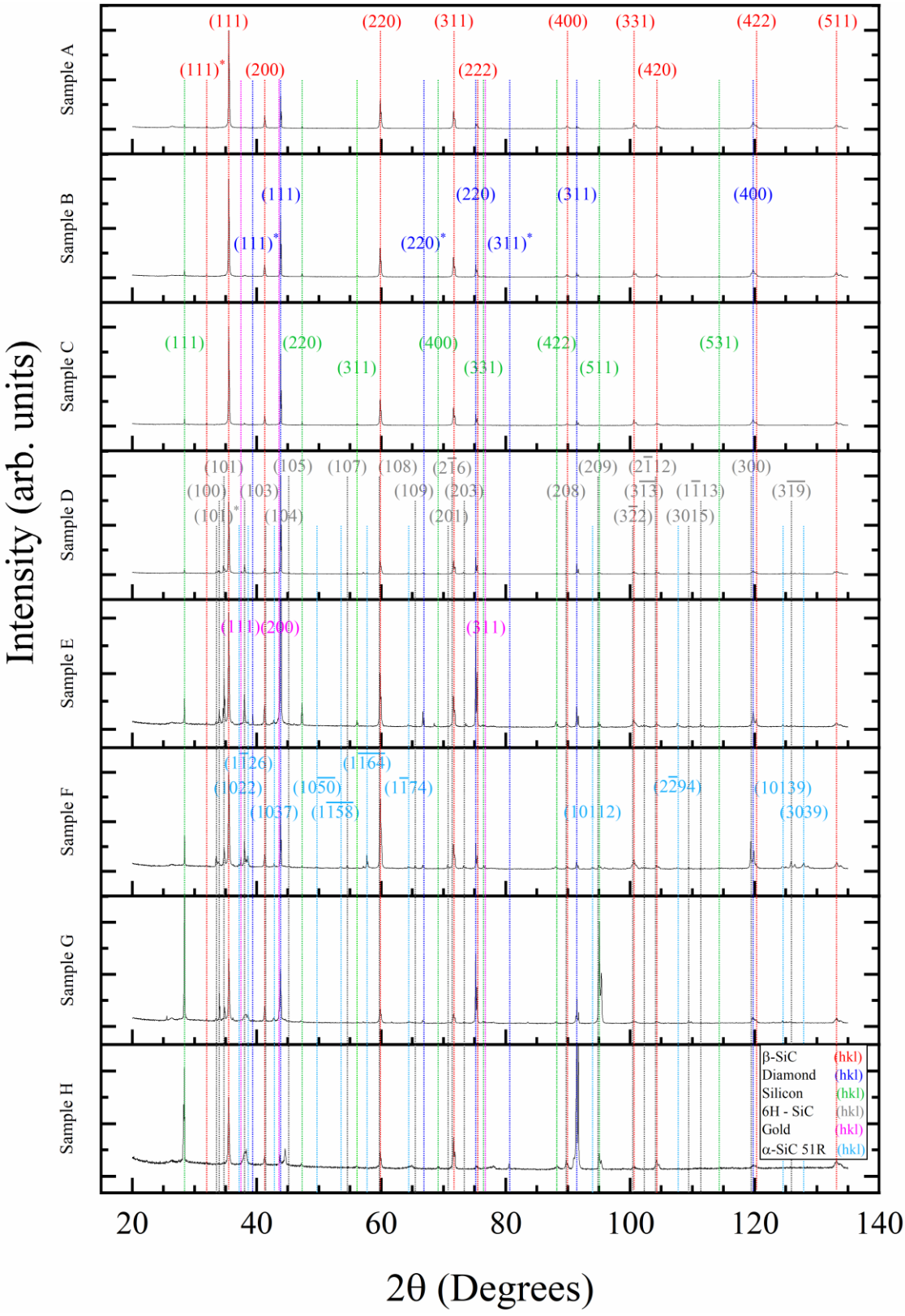

Figure 3.19 X-ray diffraction results of diamond-SiC samples ranging from 22 μm at sample A and increasing in particle size to 500 μm with sample H. The asterisk after a miller index designates Cu-kβ peaks.

3.3 Mechanisms of Heat Transfer

For nonmetals, the primary mechanism of heat transfer is by phonons. Phonons are quanta of energy associated with the vibration of a crystal lattice. In an ideal situation, the system would be comprised of a harmonic crystal and the thermal conductivity would be infinite in all directions. However, actual solids have a finite size and almost always contains defects. This means that the lattice vibrations are anharmonic in nature thus creating inelastic phonon-phonon interactions and a finite thermal conductivity. Needless to say, determining the thermal conductivity of a solid based off its anharmonic phonon-phonon interactions is exceedingly complex, involving some variables that are not generally known.

Relaxation-time approaches offer an additional method to solving the vibrational approach for thermal conductivity, however, the inelasticity of the phonon interactions challenge the assumptions of the relaxation-time model. Nevertheless, Debye developed a model based on single-mode relaxation-time. This model assumes that a temperature gradient has been applied across a certain phonon mode causing it to leave its equilibrium position and transport heat for the entirety of its lifetime while all other phonon modes remain at equilibrium. The kinetic theory result is expressed as the following equation.

$$K = \frac{1}{3} C_v^{sp} \bar{c}^2 \bar{\tau} \tag{3.1}$$

Where K is the thermal conductivity, C_v^{sp} is the phonon specific heat, c is the average phonon speed, and τ is the average phonon relaxation time.[46]

Phonon scattering is affected by several sample characteristics. At low temperatures, phonons have longer wavelengths and are thus scattered by mean free path interactions. In other words, boundary scattering dominates, and conductivity increases as temperature, T^3. Conversely, at high temperatures lattice vibrations become more anharmonic and dominate the crystal's

thermal properties, actually decreasing the material's thermal conductivity at a certain point. Point imperfections such as substitutional impurities and vacancies have one of the largest impacts on scattering phonons because the phonon wavelength is likely longer than the size of the imperfection. This type of phonon scattering is called Rayleigh type scattering such that the phonon scattering increases with the forth power of the frequency. Two-dimensional crystal defects such as dislocations, stacking faults and grain boundaries also increase phonon scattering. However, scattering from these defects is proportional to the second power of the frequency as opposed to the fourth power for one-dimensional defects. In the elastic region of dislocations there is a one to one relationship between scattering and frequency.[46]

As mentioned in the previous section, in an ideal processing situation, the samples analyzed here would be comprised of entirely silicon carbide reaction bonded with diamond. There would be no additional phases and the samples would be fully dense. From the SEM images in Section 3.1 it is clear to see that full densification has not been attained and that there are a plethora of grain boundaries and pores to adversely affect the thermal conductivity.

3.4 Thermal Conductivity Models

One of the first to derive an expression for the thermal conductivity of a heterogenous mixture was Maxwell. He assumed that the dispersed phase consisted of spherical particles with thermal conductivity k_1 and volume fraction ϕ, in a continuous matrix of thermal conductivity k_m.[47] The effective thermal conductivity of the composite, k_c is thus defined as the following:

$$\frac{k_c}{k_m} = 1 + \frac{3\phi}{\left(\frac{k_1 + 2k_m}{k_1 - k_m}\right) - \phi} \qquad 3.2$$

However, since this equation was developed for dilute media, it is only valid for low volume fractions of less than approximately 25%.[48]

Lord Rayleigh also developed equations to examine the thermal conductivity of composites. Like Maxwell, he assumed that the dispersed phase consisted of spherical particles. However, instead of these particles being randomly distributed as in the Maxwell model,[47] Rayleigh assumed that the particles were oriented in a simple cubic array in a continuous matrix and that some thermal interaction occurred between particles. Thus, the equation below is valid for higher volume fractions than those of Maxwell. With some modifications, this model can also be used to represent a composite with a simple cubic array of uniaxially arranged cylindrical fibers.[48,49]

$$\frac{k_c}{k_m} = 1 + \left(\frac{3\phi}{\left(\frac{k_1 - 2k_m}{k_1 - k_m}\right) - \phi + 1.569\left(\frac{k_1 - k_m}{3k_1 - 4k_m}\right)\phi^{\frac{10}{3}} + \cdots} \right) \qquad 3.3$$

The graph below shows the thermal conductivities of bulk and non-bulk diamond-SiC as compared to the Maxwell model. The Maxwell model was solved using the ideal case of two-phase diamond-SiC, where the thermal conductivity of diamond is 1800W/mK and the thermal conductivity of SiC is 120 W/mK.[50,51] While the graph shows that the Maxwell model seems to fit the experimental data, it cannot be considered accurate because this model assumes that a dilute media is used as the dispersed phase as well as that all phases are in intimate contact with each other. [50] Furthermore, the thermal conductivities of diamond and SiC used for this model may not accurately represent the thermal conductivities of the diamond and reaction formed SiC used in this experiment. The thermal conductivity of diamond can range between 1000 W/mK to 2500 W/mK depending on the type of diamond and how many impurities, vacancies or defects are

present.[52,53] Similarly, the thermal conductivity value of 120 W/mK used for SiC is the commercially available value.[51] This value may be different than the thermal conductivity of the polymorphs of SiC found in this experiment. In order to create a more accurate model, the thermal conductivities of each diamond particle size used in this study should be measured as well as the thermal conductivity values of the various polymorphs of SiC.

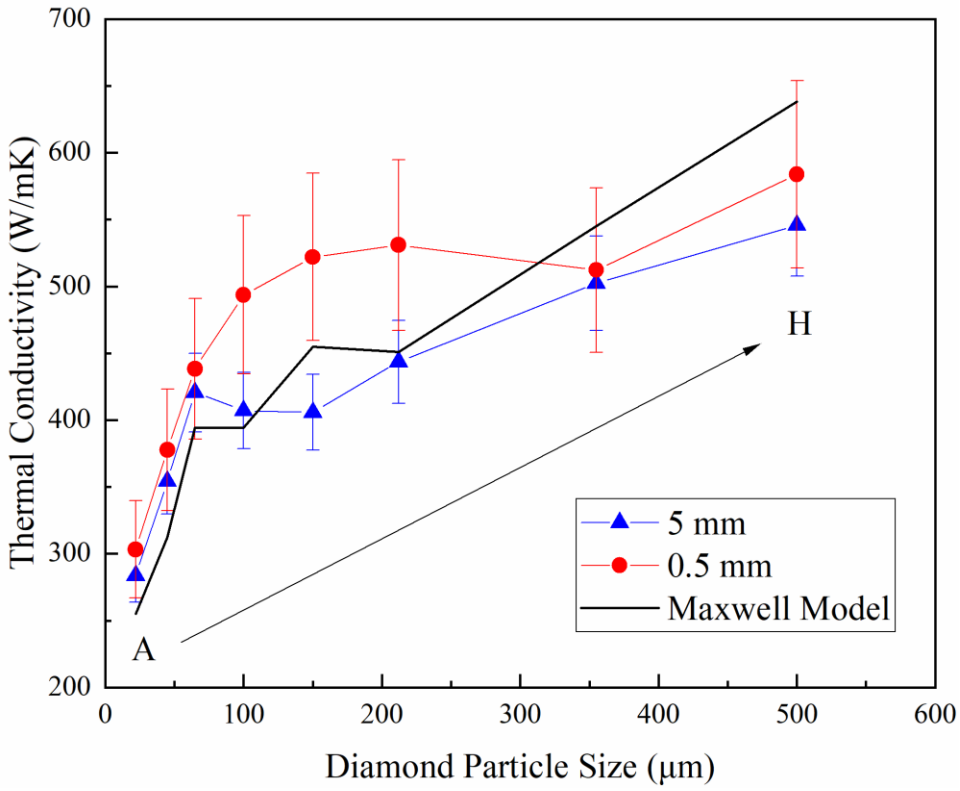

Figure 3.20 Thermal conductivity of bulk (5 mm) and non-bulk (0.5 mm) diamond-SiC as compared to the Maxwell model for dilute media thermal conductivity.

By the mid 1930's the thermal conductivity of a system comprised of liquid helium and solid copper metal was being studied. As shown through the assumptions of the Maxwell model, it was generally assumed that the thermal conductivity of the interface between the liquid helium and solid copper was small and therefore negligible. This interface was further ignored in the work of Keesom and Keesom despite their admittance that the resistance at this interface might be "relatively very considerable."[54] Nevertheless, it wasn't until 1941 when Kapitza determined that

this interface was indeed significant. He found that there was a drop in temperature, ΔT, at the interface between liquid helium and solid copper as heat flowed between them at rate Q.[55,56] The equation for the Kapitza resistance, or thermal boundary resistance is shown below.

$$R_{Bd} = \frac{\Delta T}{Q} \tag{3.4}$$

Where R_{Bd} is the thermal boundary resistance.

Further developments to predict this thermal boundary resistance are found in the Acoustic Mismatch Model (AMM) and the Diffuse Mismatch Model (DMM). Both models try to predict phonon behavior at a solid-solid interface. The AMM assumes that the phonons act as plane waves and propagate into a continuous media of isotropic Debye solids. Thus, phonons are either reflected or refracted at the interface between the two materials.[54] Below the lower Debye temperature of the two materials, the thermal boundary resistance decreases as a function of T^{-3} until becoming temperature independent.[56] Contrary to the AMM, the DMM assumes that the probability that a phonon will scatter is proportional to the density of states of each material at the interface.[54] In other words, the DMM assumes that all phonons are scattered when they reach the interface between the materials and the direction in which they scatter is determined by the density of states of the materials, rather than by the acoustic properties of the materials.[56] Unfortunately, the AMM and DMM become increasingly more error prone at temperatures above 40 K.[48]

Hasselman and Johnson developed a set of equations relating the thermal boundary resistance, expressed reciprocally as the boundary conductance h_c, to the shape and size of the dispersed media for the Maxwell and Rayleigh models for dilute volume fractions. For spherical dispersions with radius a, and volume fraction V_d, the Maxwell model was adapted to determine the effective thermal conductivity of the composite material, k_{eff}.

$$k_{eff} = k_m \frac{\left[2\left(\frac{k_d}{k_m} - \frac{k_d}{ah_c} - 1\right)V_d + \frac{k_d}{k_m} + \frac{2k_d}{ah_c} + 2\right]}{\left[\left(1 - \frac{k_d}{k_m} + \frac{k_d}{ah_c}\right)V_d + \frac{k_d}{k_m} + \frac{2k_d}{ah_c} + 2\right]} \quad 3.5$$

The boundary conductance and dispersed phase particle size were also added to the Rayleigh model to determine the effective thermal conductivity of a composite with a dispersed phase of circular cylinders oriented perpendicularly to heat flow.[57]

$$k_{eff} = k_m \frac{\left[\left(\frac{k_d}{k_m} - 1 - \frac{k_d}{ah_c}\right)V_d + \left(1 + \frac{k_d}{ah_c} + \frac{k_d}{k_m}\right)\right]}{\left[\left(1 + \frac{k_d}{ah_c} - \frac{k_d}{k_m}\right)V_d + \left(1 + \frac{k_d}{ah_c} + \frac{k_d}{k_m}\right)\right]} \quad 3.6$$

In a similar format to Hasselman and Johnson, Every and Tzou also related particle size and thermal boundary resistance of particulate composites. This adaptation however modified a model initially developed by Bruggeman for high volume fraction composites. In order to account for varying microstructures, Every and Tzou define a non-dimensional parameter, α, in relation to the Kapitza radius, a_k, and the radius of the dispersed particles, a, such that

$$\alpha = \frac{a_k}{a} \quad 3.7$$

The Kapitza radius is further defined as the product of the thermal boundary conductivity and the matrix conductivity as seen below.

$$a_k = R_{Bd} k_m \quad 3.8$$

When the Bruggeman model is modified to look at the specific scenario where the dispersed phase has a much higher thermal conductivity than the matrix, the following relationship is developed.

$$\frac{k_c}{k_m} = \frac{1}{(1-f)^{\frac{3(1-\alpha)}{1+2\alpha}}} \quad 3.9$$

Where k_c is the effective thermal conductivity of the composite and f is the volume fraction of the dispersed phase.

Every and Tzou used this model to evaluate the thermal conductivity of a composite consisting of a ZnS matrix with a diamond particle dispersed phase. In this study, the thermal conductivity of a ZnS matrix with a dispersed phase of diamond particle sizes of 0.1 μm to 0.5 μm and 0.5 μm to 4 μm were examined in relation to the volume fraction of the diamond particles in the composite. Results are shown in the figure below. The Kapiza radius of diamond particles was theoretically calculated to be 1 μm.

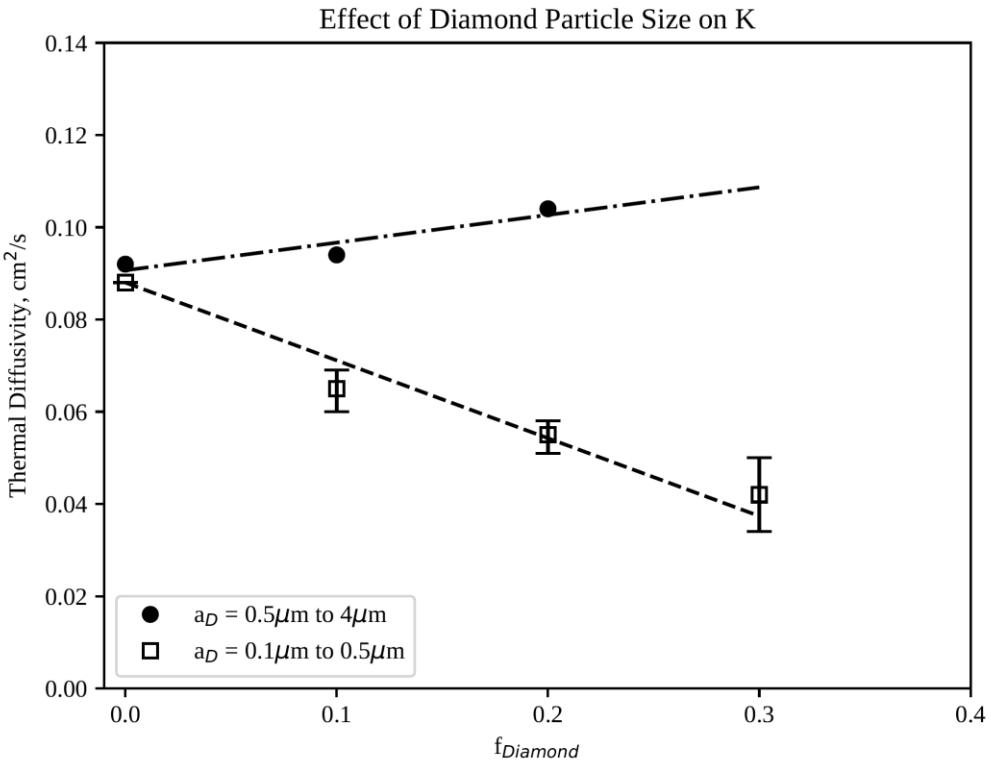

Figure 3.21 Thermal diffusivity measurements of ZnS-Diamond composite at two different particle sizes for various volume fractions.[56]

It was found that if the radius of the dispersed phase is smaller than the Kaptiza radius then the effective conductivity of the composite is reduced with increasing volume fraction of dispersed phase regardless of a high thermal conductivity attributed to the dispersed phase. Thus, in a situation with the goal to maximize the thermal conductivity of a particle based composite, the Kapitza radius offers a lower bound to the particle size that should be used as the dispersed phase.[56] While calculating the Kapitza radius for the samples tested here is out of the scope of this report, a graph of the thermal diffusivity vs. the volume fraction of mthe diamond phase is seen below. The positive slope exhibited in this graph shows that the diamond particles used for the dispersed phase are not smaller than the Kapitza radius of the material.

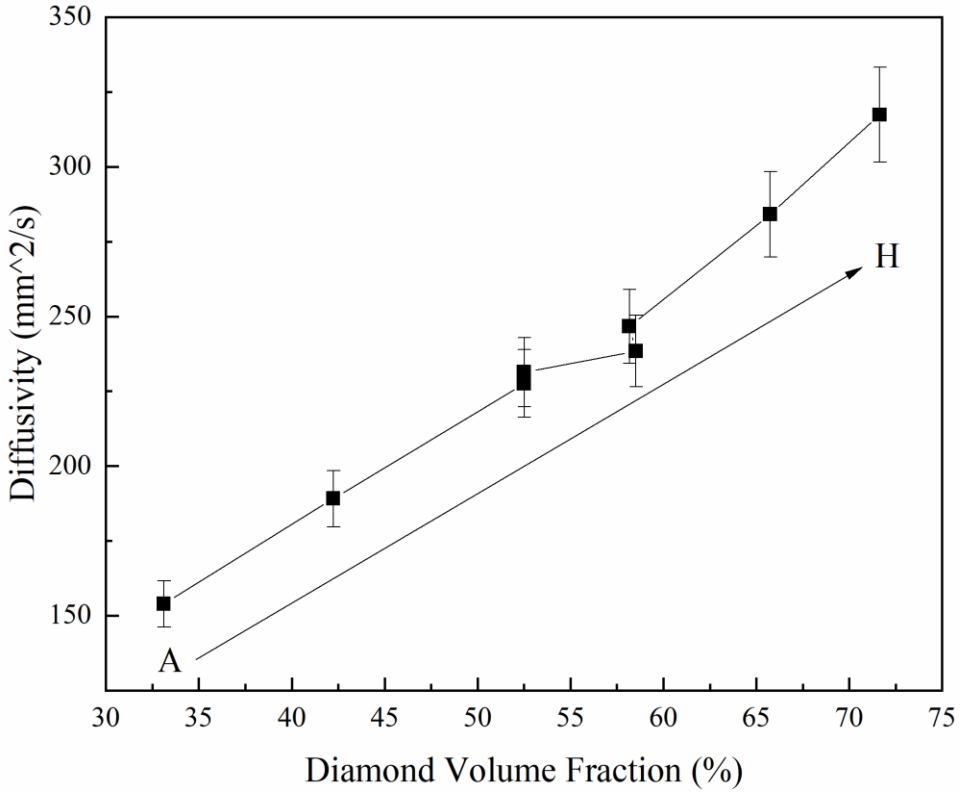

Figure 3.22 Shows thermal diffusivity as compared to volume fraction of diamond particles. Based off the work of Every and Tzou, this shows that the diamond particles used for this work are larger than the Kapitza radius.

3.5 Thermal Conductivity of Diamond-SiC

The thermal diffusivity and heat capacity of bulk and non-bulk, or 5 mm thick and 0.5 mm thick, diamond-SiC samples were measured using laser flash analysis. Equation 2.2 was used to calculate the resulting thermal conductivity, shown in the figure below.

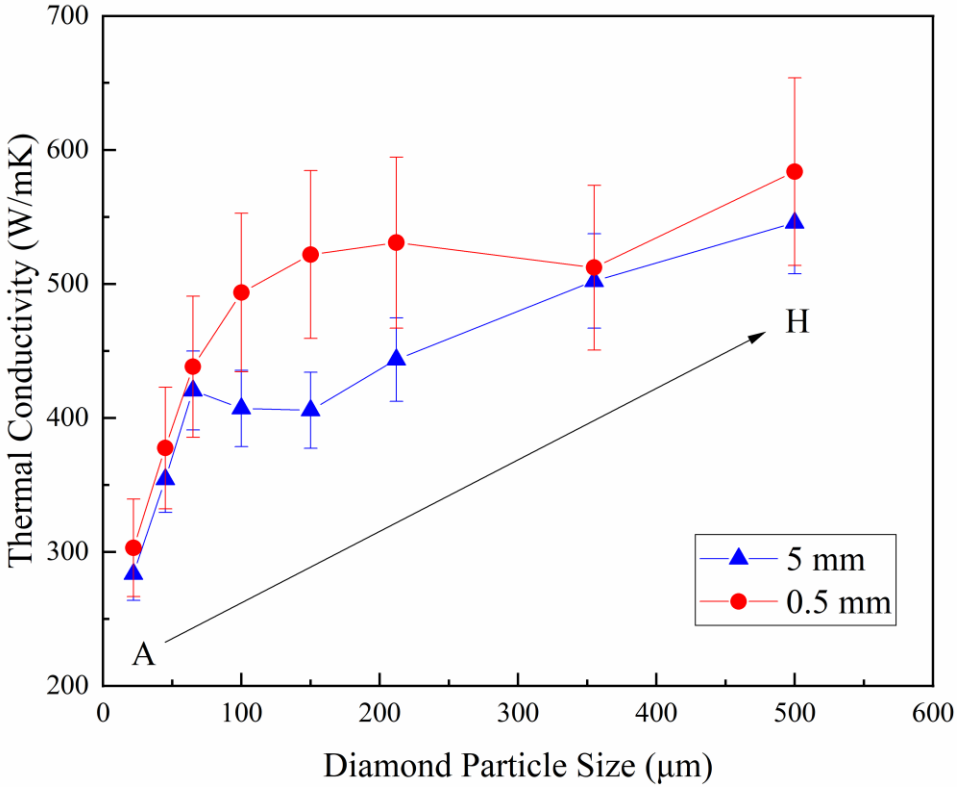

Figure 3.23 Bulk, 5 mm, and non-bulk, 0.5 mm, thermal conductivity of diamond-SiC over a range of diamond particle sizes from 22 μm to 500 μm at room temperature.

This graph shows that the non-bulk samples exhibit thermal conductivities ranging from 303 W/mK to 641 W/mK. The non-bulk samples have an interesting trend such that the thermal conductivity begins to increase linearly with grain size then proceeds in an almost parabolic way until it drops again at sample G, 355 μm. The first point to note when examining the thermal conductivity trend of the non-bulk samples is that these 0.5 mm thick disks are at the geometric limit of the assumptions for laser flash analysis and its corresponding equations. Some of the most significant assumptions in laser flash analysis is that the material is homogenous and isotropic.[25,58]

By sample D (100 μm diamond particles), the diamond particle size is so large compared to the 500 μm sample thickness that these assumptions come into question. As diamond particle size increases, the number of phonon interactions in the non-bulk samples decreases because more of the volume is apportioned to diamond and therefore there are few interfaces for scattering. One parameter that could explain the sudden decrease in thermal conductivity at sample G form 530 W/mK to 512 W/mK is the presence of silicon. The primary mechanism of heat conduction in metals is electron transport. Electron transport of thermal energy can adversely affect phonon transport as the electrons offer additional scattering mechanisms for the phonons.[46] Thus, if a significant portion of silicon is present in sample G, thermal conductivity by electrons may mask the effects of phonon transport. Sample H has the highest thermal conductivity of the set at 583 W/mK. This high thermal conductivity in the non-bulk sample is likely attributed to the fact that sample H is approximately one diamond thick. This allows the flash energy to be passed straight through the diamonds, greatly reducing the number of phonon interactions present.

The bulk samples exhibit thermal conductivities ranging from 283 W/mK to 542 W/mK and seem to exhibit the opposite trend as that in the non-bulk samples. Where the thermal conductivity of the thin samples increases at 100 μm, 150 μm and 212 μm (samples D, E, and F respectively), the thermal conductivity of the bulk samples has a negative slope for the corresponding particle sizes. This drop in thermal conductivities is likely due to the complex phases present starting with sample D, as shown in the XRD results. Samples D, E, and F have six different material phases present to scatter phonons, as well as pores. The presence of these phases is likely more noticeable in the thermal conductivity results for the bulk versus the non-bulk samples because the bulk samples have significantly more volume through witch phonon scattering can occur. The hypothesis that sample G has a higher concentration of silicon metal

dominating the phonon interactions is then reasonable because the thermal conductivities of the bulk and non-bulk sample are similar at 502 W/mK and 512 W/mK respectively.

Despite the apparent defects and multiphase induced phonon scattering, the thermal conductivities attained here are on the same order as other diamond-based composites and surpass the 400 W/mK thermal conductivity of copper when diamond particle sizes are 65 μm or higher.[1] The current highest range of thermal conductivities reported for metal-diamond composites is that of a Ag_3Si matrix. Webber has cited that a thermal conductivity of 970 W/mK has been attained with this formulation.[59] Meanwhile, aluminum-diamond composites have recently been shown to range in thermal conductivities from 525 W/mK to 700 W/mK.[50,59,60] Another diamond-SiC composite of unknown diamond particle size has also been shown to have a thermal conductivity of 600 W/mK.[61] At a maximum bulk thermal conductivity of 545 W/mK with sample H, the diamond-SiC composites made here fit within the range of those expected from other metal and ceramic diamond composites.

Chapter 4 Conclusions

The demand for high thermal conductivity materials in the electronics industry is continuing to grow with the ever increasing power density for electronic devices.[60] Binder-less liquid silicon infiltration offers an advantage to this market because it is a process capable of producing near net shape components in less time and lower temperatures than other methods while also eliminating the stress resulting from binder migration.[62] This work examines diamond-SiC composite samples ranging in size from 22 μm to 500 μm produced with the binder-less process. Infiltrated samples were laser sliced flat and parallel with Synova Laser MicroJet technology and SEM micrographs taken of the as sliced samples reveal the presence of pores and microcracks possibly resulting from solidification of SiC. X-ray diffraction results clearly show that anywhere from four to six phases of material may be present in these samples. Such phases include cubic 3C β-SiC, 6H and 51R α-SiC, diamond, silicon with a diamond structure and the possibility of gold as a residual effect of sputter coating for thermal conductivity measurements.

A review of some methods of determining composite conductivity has been discussed and the Maxwell model has been plotted against the experimental thermal conductivity data for bulk and non-bulk diamond-SiC. While the Maxwell model has a similar trend to the experimental results, it is not an accurate representation of the data for the Maxwell model applies to dispersed phase volume fractions of 25% or less and the lowest volume fraction calculated of diamond-SiC in this study is 33%. Furthermore, the Maxwell model used in this case assumes that the composite material consists of two phases.[48,50]

Laser flash analysis was used to calculate the thermal conductivity of each sample, resulting in a range of 303 W/mK to 641 W/mK and 283 W/mK to 542 W/mK for non-bulk and bulk samples respectively. In conclusion, the diamond-SiC samples produced here have thermal

conductivities on the order of that seen in aluminum-diamond and other diamond-SiC matrix composites produced today, and a thermal conductivity greater than that of copper.[1,50,60,61,63]

4.1 Future Work

Future work with diamond-SiC has almost endless bounds. First, additional processing parameters should be studied. Infiltration temperatures and times should be examined in an effort to determine if the pores in the samples are indeed from infiltration, and how to reduce them if they are. The internal stress of the samples should also be measured and compared to similar samples cast with binder. This will yield quantitative results pertaining to the reduction of stress from using a binder-less process. Furthermore, the purity of the diamonds should be examined. Weber has shown that nitrogen impurities in diamond significantly contribute to the maximum attainable thermal conductivity.[63] Thus, choosing diamonds with the fewest impurities and defects can help to maximize the thermophysical properties of the composite.

Another study of to pursue is additional work on theoretical models of thermal conductivity. While it is reasonable to suspect that there are so many defects in the current samples that the interfacial boundary resistance is overcome, it would be interesting to determine the thermal boundary resistance and Kapitza radius for these samples. Then, it would be interesting to plot the theoretical models of the Rayleigh, and Hasselman and Johnson to determine the correlation to the experimental data. One more model to experiment with is the percolation model. This model applies to composites where the dispersed phase has a significantly higher thermal conductivity than the matrix. It shows that at a certain volume fraction of dispersed media, or diamond particles in this case, a threshold is reached where the models of Maxwell, Rayleigh and Hasselman and Johnson are no longer accurate. This threshold is known as the percolation threshold. At the percolation threshold the volume fraction of the dispersed phase is so high that

the individual particles form a chain of thermal conductivity such that the resistance of the matrix phase can be neglected, seen in the drawing below. This creates pockets of high thermal conductivity thereby increasing the effective thermal conductivity of the entire sample.[64] It would be fascinating to evaluate the theoretical model and compare to the current experimental results to see if this threshold has been reached in any of the current diamond samples. If the percolation threshold has not been reached, there is an opportunity to calculate the volume fraction required to reach the percolation threshold and then determine the processing parameters to achieve this threshold with the diamond-SiC system. This would advance the goal of maximizing the thermal conductivity of diamond-SiC. Evidence suggesting that the percolation theory is attainable is seen in the figure below. This image shows that tight packing that can be achieved by some areas of the 500 μm samples which closely resembles the percolation model.

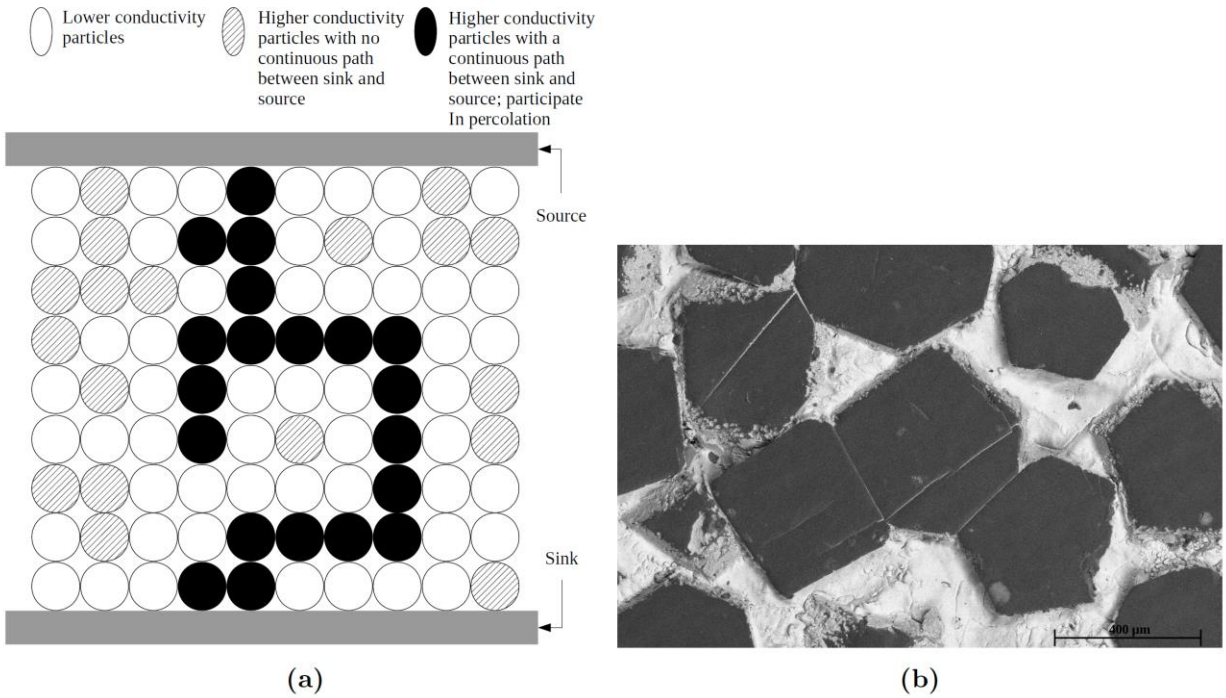

Figure 4.1 Shows an example of a percolation pathway in (a). (b) shows the potential of percolation in 500 μm diamond-SiC.[64]

References

1. Ho, C. Y., Powell, R. W. & Liley, P. E. Thermal Conductivity of the elements. *J. Phys. Chem. Ref. Data* **1,** 332 (1972).
2. May, P. W. Diamond thin films: a 21st-century material. *Phil. Trans. R. Soc. Lond. A* **358,** 473–495 (2000).
3. Wörner, E., Wild, C., Müller-Sebert, W., Locher, R. & Koidl, P. Thermal conductivity of CVD diamond films: high-precision, temperature-resolved measurements. *Diam. Relat. Mater.* **5,** 688–692 (1996).
4. Bain Company Inc. & AWDC. *The Global Diamond Industry - Lifting the Veil of Mystery*. (2011).
5. Tennant, S. On the Nature of the Diamond. *Philos. Trans. R. Soc. London* **87,** 123–127 (1797).
6. Jerome T. Coe & Coe, J. T. *Unlikely Victory: How General Electric Succeeded in the Chemical Industry*. *Lexan Polycarbonate: 1953-1968* (2010).
7. Thomas, M. & Tropf, W. Optical Properties of Diamond. *Johns Hopkins APL Tech. Dig.* **14,** 16–23 (1993).
8. Tönshoff, H. K., Hillmann-Apmann, H. & Asche, J. Diamond tools in stone and civil engineering industry: Cutting principles, wear and applications. *Diam. Relat. Mater.* **11,** 736–741 (2002).
9. Cape, J. A. & Lehman, G. W. Temperature and finite pulse-time effects in the flash method for measuring thermal diffusivity. *J. Appl. Phys.* **34,** 1909–1913 (1963).
10. Seal, M. & van Enckevort, W. J. P. Applications of Diamonds in Optics. in *SPIE* **969,** 189–193 (1988).
11. Yang, W. *et al.* DNA-Modified Nanocrystalline Diamond Thin Films as Stable, Biologically Active Substrates. *Nat. Mater.* **1,** 253–257 (2002).
12. Chen, P. H., Lin, C. L., Liu, Y. K., Chung, T. Y. & Liu, C. Diamond Heat Spreader Layer for High-Power Thin-GaN Light-Emitting Diodes. *IEEE Photonics Technol. Lett.* **20,** 845–847 (2008).
13. Ring, T. A. *Fundamentals of Ceramic Powder Processing and Synthesis*. (Academic Press, Inc., 1996).
14. Technologies), (Pace. *Safety Data Sheet for Phenolic Compression Mounting Resin (All Colors)*. (2009).
15. Chemicals), (Georgia-Pacific. *Material Safety Data Sheet for GP 5018 RESI-SET Phenolic Impregnating Resin*. (2013).
16. Comeforo, J. E. Migration Characteristics of Organic Binders. *Ceram. Age* 132–135 (1945).
17. Front, F., Protas, B., Richardson, J. & Foster, J. M. Binder Migration During Drying of Lithium-Ion Battery Electrodes: Modelling and Comparison to Experiment. *J. Power Sources* **393,** 177–185 (2018).
18. Kell, G. S. Density, Thermal Expansivity, and Compressibility of Liquid Water from 0° to 150°C: Correlations and Tables for Atmospheric Pressure and Saturation Reviewed and Expressed on 1968 Temperature Scale. *J. Chem. Eng. Data* **20,** 97–105 (1975).

19. Synova. Metal Cutting System Cool Laser Machining Advanced Laser Cutting Systems Synova Laser MicroJet ® Technology Materials & Operations.

20. Synova. SYNOVA: The Laser MicroJet Technology. (2017).

21. SIBAILLY, O., WAGNER, F., MAYOR, L. & RICHERZHAGEN, B. High precision laser processing of sensitive materials by Microjet. **5063,** 501–504 (2003).

22. Perrottet, D., Amorosi, S. & Richerzhagen, B. New process for screen cutting: water-jet guided laser. **5961,** 596105 (2005).

23. Poirier, D. R. & Geiger, G. H. *Transport Phenomena in Materials Processing*. *Journal of Experimental Psychology: General* **136,** (The Minerals, Metals & Materials Society, 1994).

24. Campbell, R. *Thermophysical Properties Section Prepared by*. (2018).

25. Parker, W. J., Jenkins, R. J., Butler, C. P. & Abbott, G. L. Flash method of determining thermal diffusivity, heat capacity, and thermal conductivity. *J. Appl. Phys.* **32,** 1679–1684 (1961).

26. Koski, J. A. Improved Data Redution Methohds for Laser Pulse Diffusivity Determination with the Use of Minicomputers. *Proc. Eighth Symp. Thermophys. Prop.* **II,** 94–103 (1982).

27. Donaldson, A. B. & Taylor, R. E. Thermal diffusivity measurement by a radial heat flow method. *J. Appl. Phys.* **46,** 4584–4589 (1975).

28. Shaffer, P. T. B. Refractive Index, Dispersion, and Birefringence of Silicon Carbide Polytypes. *Appl. Opt.* **10,** 1034 (1971).

29. Spitzer, W. G., Kleinman, D. & Walsh, D. Infrared properties of hexagonal silicon carbide. *Phys. Rev.* **113,** 127–132 (1959).

30. Leng, Y. *Materials Characterization Introduction to Microscopic and Spectroscopic Methods*. (Wiley-VCH Verlag GmbH & Co., 2013).

31. Bearden, J. A. *X-Ray Wavelengths and X-Ray Atomic Energy Levels,*. **31,** (1967).

32. Momma, K. & Izumi, F. VESTA 3 for three-dimensional visualization of crystal, volumetric and morphology data. *J. Appl. Crystallogr.* **44,** 1272–1276 (2011).

33. Match! Phase Identification from Powder Diffraction. (2018).

34. Callister, W. D. *Materials Science and Engineering An Introduction*. *New England Journal of Medicine* **344,** (John Wiley & Sons, Inc., 2007).

35. Liu, R. J., Cao, Y. B., Yan, C. L., Zhang, C. R. & He, P. B. Preparation and characterization of diamond-silicon carbide-silicon composites by gaseous silicon vacuum infiltration process. *J. Superhard Mater.* **36,** 410–414 (2014).

36. Mlungwane, K., Herrmann, M. & Sigalas, I. The low-pressure infiltration of diamond by silicon to form diamond-silicon carbide composites. *J. Eur. Ceram. Soc.* **28,** 321–326 (2008).

37. Ramsdell, L. S. Studies of Silicon Carbide. *Am. Mineral.* **32,** 64–82 (1947).

38. Wyckoff, R. G. W. *Crystal Structures Vol. 1*. (Interscience Publishers, 1963).

39. Fayos J. Possible 3D Carbon Structures as Progressive Intermediates in Graphite to Diamond Phase Transition. *J. Solid State Chem.* **148,** 278–285 (1999).

40. Dutta, B. N. Lattice Constants and Thermal Expansion of Silicon up to 900C by X-Ray Method. *Phys. Status Solidi* **2,** 984–987 (1962).

41. Suh, I. K., Ohta, H. & Waseda, Y. High-Temperature Thermal Expansion of Six Metalic Elements Measured by Dilation Method and X-Ray Diffraction. *J. Mater. Sci.* **23,** 757–760 (1988).

42. Ott, H. Die Gitterstruktur des Karborunds (Si C) I. *Zeitschrift fuer Krist. Krist. Krist. Krist.* **61,** 515–531 (1925).

43. Ramsdell, L. S. The Structure of alpha-SiC, Type V. in *Proceedings of the Twenty-Sixth Annual Meeting of the Mineralogical Society of America at Pittsburgh, Pennsylvania* (ed. Hunrnut, C. S.) 205 (American Mineralogist, 1946).

44. Salamone, S. & Spriggs, O. Effect of Reaction Time on Composition and Properties of SiC-Diamond Ceramic Composites. *CESP* **32,** 213–222 (2011).

45. Tang, C. J. *et al.* Effect of nitrogen and oxygen addition on morphology and texture of diamond films (from polycrystalline to nanocrystalline). **17,** 72–78 (2008).

46. Shinde, S. & Goela, J. *High Thermal Conductivity Materials*. (Springer Science+Business Media, Inc., 2006).

47. Maxwell, J. *A Treatise on Electricity and Magnetism*. *Oxford at the Clarendon Press* **1,** (1873).

48. Pietrak, K. & Wisniewski, T. S. A Review of Models for Effective Thermal Conductivity of Composite Materials. *J. Power Technol.* **95,** 14–24 (2015).

49. Rayleigh, Lord. LVI. *On the influence of obstacles arranged in rectangular order upon the properties of a medium*. *Philos. Mag. Ser. 5* **34,** 481–502 (1892).

50. Flaquer, J., Ríos, A., Martín-Meizoso, A., Nogales, S. & Böhm, H. Effect of diamond shapes and associated thermal boundary resistance on thermal conductivity of diamond-based composites. *Comput. Mater. Sci.* **41,** 156–163 (2007).

51. Rashed, A. H. & (Poco Graphite, I. . Properties and Characteristics of Silicon Graphite. 1–8 (2002).

52. Graebner, J. E. Thermal Conductivity of Diamond. *Diam. Electron. Prop. Appl.* 285–318 (1995). doi:10.1007/978-1-4615-2257-7_7

53. Kidalov, S. V. & Shakhov, F. M. Thermal conductivity of diamond composites. *Materials (Basel).* **2,** 2467–2495 (2009).

54. Swartz, E. T. & Pohl, R. O. Thermal Boundary Resistance. *Rev. Mod. Phys.* **61,** 605–668 (1989).

55. Kapitza, P. L. The study of heat transfer in helium II. *J. Phys.(USSR)* **4,** 181–210 (1941).

56. Every, A. G., Tzou, Y., Hasselman, D. P. H. & Raj, R. The Effect of Paricle Size on the Thermal Conductivity of ZnS/Diamond Composites. *Acta Metall. Mater.* **40,** 123–129 (1992).

57. Hasselman, D. P. H. & Johnson, L. Effective Thermal Conductivity of Composites with Interfacial Thermal Barrier Resistance. *J. Compos. Mater.* **21,** 508–515 (1987).

58. Conshohocken, W. Standard Test Method for Thermal Diffusivity by the Flash Method 1. **i,** 1–11 (2014).

59. Weber, L. & Tavangar, R. Diamond-Based Metal Matrix Composites for Thermal Management Made by Liquid Metal Infiltration — Potential and Limits. *Adv. Mater. Res.* **59,** 111–115 (2009).

60. Ruch, P. W., Beffort, O., Kleiner, S., Weber, L. & Uggowitzer, P. J. Selective interfacial bonding in Al(Si)-diamond composites and its effect on thermal conductivity. *Compos. Sci. Technol.* **66,** 2677–2685 (2006).

61. Mcclarence, E. & (ElementSix). A precious mixture. *Mater. World* 30–31 (2007).

62. Chiang, Y. M., Messner, R. P., Terwilliger, C. D. & Behrendt, D. R. Reaction-formed silicon carbide. *Mater. Sci. Eng.* **144,** 63–74 (1991).

63. Monachon, C. & Weber, L. Effect of diamond surface orientation on the Thermal Boundary Conducance between diamond and aluminium. *Diam. Relat. Mater.* **39,** 8–13 (2013).

64. Devpura, A., Phelan, P. E. & Prasher, R. S. Percolation theory applied to the analysis of thermal interface materials in flip-chip technology. in *ITHERM 2000. The Seventh Intersociety Conference on Thermal and Thermomechanical Phenomena in Electronic Systems (Cat. No.00CH37069)* **1,** 21–28 (2000).